# Atomistic damage mechanisms during hypervelocity projectile impact on AlN: A large-scale parallel molecular dynamics simulation study

Paulo S. Branicio[a,b], Rajiv K. Kalia[a], Aiichiro Nakano[a], Priya Vashishta[a,*], Fuyuki Shimojo[c], Jose P. Rino[b]

[a]*Collaboratory for Advanced Computing and Simulations, Departments of Chemical Engineering and Materials Science, Physics and Astronomy, and Computer Science, University of Southern California, Los Angeles, CA 90089-0242, USA*
[b]*Department of Physics, Universidade Federal de São Carlos, São Carlos, SP 13565-905, Brazil*
[c]*Department of Physics, Kumamoto University, Kumamoto 860-8555, Japan*

## Abstract

Atomistic mechanisms of damage initiation during hypervelocity (15 km/s) impact on an AlN coating is investigated using parallel molecular-dynamics simulations involving 209 million atoms. On impact a strong shock wave is generated, which then splits into an elastic precursor and a structural phase transformation (SPT) waves, the latter driving a wurtzite to rocksalt structural transition. During its development, the SPT wave induces plastic processes in the intact wurtzite material, which in turn facilitate the nucleation and growth of brittle cracks. Specifically, the interface between the transformed (rocksalt) and untransformed (wurtzite) regions acts as a source of nanocavities and kink bands. They further interact with stress release waves reflected from the back surface and create cracks in mode I, from the nanocavities, and in mode II, from the kink band superdislocation boundary. Stresses are evaluated using a stoichiometric-preserving formula for virial local averages on inhomogeneous binary systems. Defects are analyzed using shortest-path ring statistics.
© 2007 Elsevier Ltd. All rights reserved.

*Keywords:* A. Shock waves; B. Ceramic material; C. Solid–solid transitions; D. Kink bands; E. Fracture mechanisms

## 1. Introduction

High-strength ceramics such as $B_4C$, $Si_3N_4$, $Al_2O_3$, SiC and AlN are of great technological importance for the design of better light-weight coatings and tiles, e.g. for satellites, spacecrafts, space stations, vehicles and personal armor (Levinshteæin et al., 2001; Pechenik et al., 1999; Sheppard, 1990). These ceramics have outstanding mechanical properties, such as high hardness and strength, and lower densities than metals, which make them ideal light-weight coating materials. Under impact compression these ceramics are very strong, what allows them to form a rigid barrier and effectively break impacting projectiles. However, they are brittle

*Corresponding author. Tel.: +1 213 821 2663; fax: +1 213 821 2664.

*E-mail address:* priyav@usc.edu (P. Vashishta).

and weak under tension, and their efficiency can be seriously degraded by fracture. Understanding the mechanisms of impact damage of high-strength ceramics leading to crack propagation and fracture is thus essential. Nevertheless, their behavior at extreme gradients of temperature and pressure produced during high speed impacts is not completely understood.

For most high-strength ceramics, the longitudinal sound speed is less than 10 km/s. At moderate impact speeds below this value, a variety of studies (Bourne, 2006; Chen et al., 2003, 2006; Millett et al., 2005; Orphal et al., 1996; Reaugh et al., 1999; Reinhart et al., 2006; Riou et al., 1998; Strassburger et al., 1994; Vogler and Chhabildas, 2006; Yadav and Ravichandran, 2003) have been carried out to understand the damage generation and evolution under projectile and plane impacts. On impact, a large amount of energy is rapidly released, generating local stress and temperature gradients which propagate in the target as a compressive shock wave. The mechanical response of the ceramics to this scenario depends on their intrinsic material properties and the projectile speed that affects the rate of energy transferred to the target and the strength of the shock wave. Recently, the formation of shock-induced amorphization bands was observed during projectile impacts at speed below sound velocity in $B_4C$. Chen et al. (2003) described these bands in $B_4C$ as the mechanism leading to crystalline failure and loss of ballistic performance.

At hypervelocity impacts, i.e. at velocities above the longitudinal sound speed, the scenario is even more complex. At these speeds, the response of ceramics includes explosive effects due to the extreme high gradients in density, stress, and temperature. Impacts in this speed range are common in space, where micro-meteoroids travel with speeds up to 40 km/s, posing a threat to satellites, spacecrafts, and space stations. Quasi-static indentation studies have been applied to describe the meteoroid impact damage in space solar cells (Herbert et al., 2001), but a full description of the complex response under these conditions can only be accessed by hypervelocity impact experiments. This kind of experiment is however still incipient.

The damage mechanisms can become very intricate in certain high-strength ceramics, such as SiC and AlN, which undergo a structural phase transformation (SPT) under high pressure. Such SPT have shown to be important in a wide variety of solids materials (Branicio et al., 2006b; Karki et al., 2001; Mota et al., 2006; Wentzcovitch et al., 1998; Yang et al., 2006). For AlN, experimental and theoretical studies have shown that it transforms from the wurtzite to the rocksalt structure at pressures in the range 12.5–22.9 GPa (Christensen and Gorczyca, 1993; Gorczyca et al., 1991; Kipp and Grady, 1994; Mashimo et al., 1999; Uehara et al., 1997; Ueno et al., 1992; Xia et al., 1993). If the compressive shock wave is strong enough to reach this pressure during the impact, this transformation could be activated and, in theory, play a role in damage initiation, though no specific mechanism has been proposed (Chen et al., 2003).

In the absence of experimental information, numerical simulations are expected to play an important role in the study of hypervelocity impact on high-strength ceramics. Numerically, shock-impacted materials have been studied primarily by continuum simulations based on the finite elements method (FEM) (Beissel et al., 2006; Gorelskii et al., 2000; Holmquist and Johnson, 2006; Holmquist et al., 2000a, b, c, 2001; Johnson and Holmquist, 1999; Mcdonald et al., 1993; Pandolfi et al., 2006; Quan et al., 2006; Tasdemirci and Hall, 2007; Wilkins, 1978), which use constitutive equations to inter-relate stresses, strength, and the degree of damage. A limitation of FEM simulations is the lack of knowledge on the microscopic mechanisms of damage initiation, in order to determine the time and location of crack nucleation at the atomistic level. Atomistic simulations based on the molecular dynamics (MD) method provide the trajectories of all the atoms, and thus are expected to shed light on the atomistic mechanisms of damage initiation, leading to failure (Holian, 2002).

In this paper, we describe a large-scale MD simulation of hypervelocity projectile impact on AlN ceramic. A speed of 15 km/s in the hypervelocity range is used to investigate the interplay between stress waves and SPT, and their relation to incipient crack development. A large system involving 209 million atoms is used to enable the requisite coupling between long-range wave phenomena and atomistic damage initiation mechanisms. The ceramic chosen, AlN, is a promising high-strength ceramic, which is receiving increasing attention. Compared to other high-strength ceramics, AlN has the best performance in the high-speed impact range. Experiments by Reaugh et al. (1999) showed that AlN, among other high-strength materials, best prevents the penetration of cylindrical tungsten projectiles at speeds higher than 2.5 km/s. A short letter discussing some of these results was published in the *Physical Review Letters* (Branicio et al., 2006a).

The paper is organized as follows. In Section 2, we summarize important advances in the study of impact on ceramics, focusing mainly on projectile impact on AlN. Some of the most relevant experimental, continuum

and atomistic simulation studies in this area are discussed in this section. In Section 3, we describe the methodology employed. We discuss the interaction potential for AlN and its validation, the parallel MD method, the calculation of properties, and data visualization. In Section 4, we describe the simulation results, and finally in Sections 5 and 6, we present discussions and summarize our main conclusions, respectively.

## 2. Preliminaries

Before describing the methodology used in this work and discussing the results obtained, it is important to recall the current state of the art and review some of the major theoretical and experimental studies of this area. High velocity impact is a research field of great interest to military and civilian applications. Most studies are traditionally performed at military facilities in the development of better projectiles and armor. However, high-speed impacts are essential in several other areas. For instance, in high-pressure physics, the main focus is the description of materials equation of state at high pressure and high temperature, usually only accessible through the use of high-speed impacts. Impacts in this range are also of interest to space applications where objects can be found traveling at hypervelocity speeds and the effects of impacts need to be known to access the risk for spaceship traveling and better design effective protection systems. The formation of craters and debris cloud from impacts is also an interesting field of study by itself and of great importance to the study of interplanetary dust particles and orbital debris. Below we discuss some of the main studies of high velocity impact on materials. We highlight important experiments and simulations, using continuum and atomistic approaches, focusing on impacts in high-strength ceramics and composites, especially AlN.

### 2.1. Experimental studies of projectile impact

The main subjects of experimental studies in the high-speed impact field are the determination of the performance of materials and the description of damage mechanisms. However, several specific issues have been challenging experimentalists and are the subjects of several studies. Among them are the effects of the projectile shape and weight, the induced fracture pattern, damage in solar cells, and the performance of material composites and layering. Below we discuss briefly several studies focusing these subjects.

The effect of geometry and mass of the projectile on the induced target damage is a key issue investigated by Hohler and Stilp (1987). They experimentally investigated this problem performing hypervelocity impacts of metallic cylinder rod projectiles with a wide range of length to diameter ($L/D$) ratio, from 1 to 32. $L/D$ ratio was shown to determine the velocity dependence of crater depth, diameter and volume on metallic targets. For high impact velocity, the crater depth of short rods ($L/D \sim 1$) was shown to be approximately proportional to $v_p^{2/3}$ ($v_p$, projectile velocity). Increasing the $L/D$ ratio, the slope of the penetration curves decrease and converges to a value nearly independent of $v_p$ for rods with $L/D \gg 1$. Above this value, the projectile efficiency is only obtained by increasing the projectile mass, not the velocity. The specific effects of long rods on $B_3C_4$ ceramics was investigated by Orphal et al. (1997). They measure the impact of tungsten rods in the velocity range 1.5–5.0 km/s. To reach the maximum velocity they use a two-stage light-gas-gun. They used several flash X-rays to obtain independent views of the projectile-target interaction during the penetration and showed that penetration of the target is essentially steady-state with a constant consumption rate of the projectile over the whole velocity range. The total penetration depth equals or slightly exceeds the theoretical hydrodynamics value for velocities above 4 km/s.

The fracture profiles on ceramics induced by projectile impact were investigated by Strassburger et al. (1994) SiC, $TiB_2$, and $Al_2O_3$ ceramics were impacted, in the edge-on geometry, by steel projectiles in the velocity range 0.02–1 km/s, with a Cranz–Schardin high-speed camera recording pictures of the incipient fracture propagation. They observed two types of crack profiles: (I) distinguishable fuzzy cracks inside a cone of propagation starting from the front face to the target rear; and (II) a cone of cracks with a crack front with a high density of crack traces. $TiB_2$ showed only crack profile II, whereas SiC and $Al_2O_3$ showed both profiles. At low velocities profile I is predominant but for velocities above 0.35 km/s profile II is observed. In a similar experiment, Riou et al. (1998) performed impacts of steel projectiles in the $v_p = 0.1$–0.35 km/s velocity range on SiC ceramics in the beam geometry. The results showed, for $v_p = 0.203$ km/s, the presence of a cracked zone with a conical shape with a high cracked density and a circular crack front propagating towards the rear

face of the target. For $v_p = 0.25$ km/s, additional transverse cracks (called spalls) result from the tensile reflection of the compressive wave on the rear surface of the target. For $v_p = 0.32$ km/s, additionally several small cracks were observed. For $v_p = 0.26$ km/s and confined SiC target, the crack profile was quite similar to unconfined SiC. The presence of confinement seems to limit the initiation of transverse cracks, which appear for an unconfined beam configuration but does not interfere with the initial damage profile. They pointed out that damage is induced by the initial tensile state, which is independent of confinement.

Hypervelocity impacts in solar cells in space were characterized by Herbert et al. (2001). They compared the damage induced by quasi-static indentation to those created by hypervelocity impact of micrometeoroids in solar cells of the Hubble Space Telescope. The analysis showed that damage morphologies share some common fracture features. Using a blunt indentation the target response is analogous to that under hypervelocity impact with circumferential fracture preceding any radial fracture, and similar cone-spallation geometries and preferential fracture planes. They showed that quasi-static indentation with energies of $\sim 1/100$ of the hypervelocity impact still induce consistent morphologies of damage though additional work is needed to access the flux of impacting space debris and meteoroid particles causing the damage.

The projectile impact performance of ceramic–metal composites was investigated by Strassburger et al. (2000). Two $Al_2O_3$–Al composites with ceramic volume fraction of 70% (cermet 1) and 84% (cermet 2) were impacted in the edge-on geometry. They used a Cranz–Schardin high-speed camera and flash X-ray radiography to monitor the deformation of the targets and the projectiles residual velocities. Cermet 1 showed lower performance than reference alumina, based on residual velocity and ballistic limit data, whereas the resistance performance of cermet 2 is equal or better than the pure ceramic. Two major differences in fracture behavior were observed, a delay in fracture formation, and a damage velocity half of that of the reference ceramic. The effect of polymer bonding in the performance of a ceramic layered structure was studied by Yadav and Ravichandran (2003). They performed projectile impacts of tungsten alloy rods in the 1–1.2 km/s velocity range against ceramic-/polymer-laminated structures. The laminated structure was made of several layers of AlN ceramic with thin layers of polyurethane in between. The results indicate that unconfined ceramic structure penetration resistance can be improved significantly using the laminated ceramics structure. The enhanced performance is attributed to a reduced wave propagation velocity in the laminated structure and also to the crack arresting feature of the polymer layer.

The behavior of AlN targets under impact was the subject of several investigations. Orphal et al. (1996) studied the impact and penetration of long tungsten rods in the 1.5–4.5 km/s velocity range in AlN confined targets and showed very similar results as found in impacts on $B_3C_4$ (Orphal et al., 1997). Target penetration and consumption rate of the projectile rod was essentially steady-state over the entire impact velocity range, while the total penetration depth for velocities above 4 km/s exceeded the theoretical hydrodynamics value. In another study, Kipp and Grady (1994) showed that SPT in AlN could be generated dynamically using projectile impacts. They used tungsten and tantalum projectiles, impact velocities of 2.2 km/s, and a confined thin AlN ceramic plate. Their results indicate that the transition from the wurtzite (hexagonal) to the rocksalt (cubic) structure starts at 22 GPa, accompanied by a volume reduction of about 20%. Using velocity interferometry, the shock wave profile was measured indicating clearly the shock wave split in the elastic, plastic and transformation components. A ballistic performance study of tiles made of five ceramic materials ($Al_2O_3$, SiC, $B_3C_4$, AlN, $TiB_2$) and Pyrex was done by Reaugh et al. (1999). They used impact velocities from 1.35 to 2.6 km/s. They showed from the minimum thickness necessary to prevent the complete penetration of the tile, that the limiting areal density for each ceramic increases linearly with velocity, with different rates for each material. In particular the limiting areal density of AlN has the slowest increase with velocity of all the materials tested. As a consequence, it is the best performer at high velocity, i.e. requires the least areal density to stop the projectile. Results also showed that the use of two plates to obtain a desired thickness instead of a single plate has insignificant effects on performance, but if two layers of different materials are used then the order in which they occur might strongly influence their performance especially if the materials individually have very different performances.

Recently, new mechanisms of damage initiation in $B_4C$ were described at the high velocity impact range by Chen et al. (2003). The results indicated the formation of intragranular shock-induced amorphization bands preceding fracture development during projectile impacts at 0.9 km/s. The amorphous bands were shown to be localized along specific crystallographic directions and with apparent cleaved fracture surfaces. The

mechanism could explain the unclear decrease in the ballistic performance of boron carbide at high rates and pressures. The experimental verification of localized amorphization of boron carbide during shock loading illustrates the complex effects that can result from the rapid exposure of a material to extreme conditions of high pressure and temperature.

## 2.2. Continuum simulations of projectile impact

Continuum simulation methods, such as the FEM, have played an important hole in the understanding of the important parameters and mechanisms involved in the complex problem of high-speed projectile impact damage on high performance targets. A great advantage of the continuum methods is that they enable the simulation of structures of realistic size, providing a direct link with experimental data. The major limitation of them, however, is their rather limited predictive capability. Also, equilibrium bulk and surface material properties are often assumed, despite the fact that these properties may change in regions of high deformations. Recently, several alternative approaches and constitutive models were designed to overcome some of these difficulties, providing more accurate procedures to simulate the dynamic damage in high performance ceramics such as AlN.

Continuum simulations of projectile impact started to get attention with the pioneer work of Wilkins and collaborators (Wilkins, 1978). Wilkins performed FEM simulations of the penetration of steel projectiles in aluminum targets. The simulation results provided clear evidences to identify the important parameters involved in the performance of both the projectile, that should defeat the target using the minimum energy, and of the target that should defeat the projectile using the minimum areal density (minimum thickness). In his work, Wilkins highlight the importance of high velocity, high density and the length of the projectile in the direction of penetration as critical parameters of a good projectile. For the target, besides the density and thickness, the other important parameters identified are the high bulk and shear modulus, high yield stress, and resistance to fracture when large tensile stresses develop.

A continuum simulation based on a hydrodynamic code was employed by Mcdonald et al. (1993), to study the hole size formation caused by hypervelocity aluminum cubes hitting on thin aluminum films. The time evolution of density, pressure, and temperature for impacts at 7, 9 and 11 km/s showed that the hydrocode give results consistent with experiments. Another FEM simulation of hypervelocity impact was performed by Gorelskii et al. (2000), simulating the destruction of ceramics plates by steel cylinders. They used impact speeds from 0.6 to 4 km/s and simulated the impact using an FEM constitutive model including the possibility of incipient and developing cracks. Their FEM results are consistent with experimental data and show that for velocities below 1.0 km/s, the impact induces only deformation on the steel cylinder in the contact zone. Although for velocities above 1.5 km/s, the cylinder is able to penetrate the ceramic target, and finally for velocities about 4.0 km/s appreciable erosion and destruction of the sample is observed.

The FEM approach to projectile impact simulations acquired a new level of accuracy with the introduction of sophisticated particle (meshless) algorithms to simulate high velocity impact. Beissel et al. (2006) and Johnson et al. (1996) proposed and employed the smooth particle hydrodynamics (SPH) technique in order to provide more flexible conditions on the continuum simulated behavior of the grid nodes making this a continuum method convenient for high distortion impact computations. SPH nodes could link with standard finite elements making the simulation convenient to describe both highly distorted flow and structural response. The application of the method to high velocity impact is inherently superior to the usual straight application of conventional FEM as the nodes connectivity is dynamic in the SPH, in contrast with the static connectivity of standard finite elements, making the simulation of highly deformed regions in the impact zone and the plastic flow more realistic. A close but improved version of the SPH method was provided by Johnson et al. (2000). The generalized particle algorithm (GPA), an extension of the SPH method, provides a sophisticated meshless algorithm with variable nodal connectivity designed to simulate materials under a number of severe distortion conditions.

Apart from the methodological development of the continuum methods for projectile impact simulations, the development of constitutive modeling of ceramics also advanced with the development of a model for brittle materials subjected to large strains, high strain rates and high pressure proposed by Johnson and Holmquist (1999). The capabilities of the model were demonstrated describing the response of $B_4C$ under

projectile impact. The calculated strength, pressure, and damage profile on plate impact, high velocity penetration, and thin plate perforation were consistent with experimental results.

A constitutive model for the wurtzite phase of AlN was developed by Holmquist et al. (2000b, 2001). They used the Johnson–Holmquist model (JH-2) for brittle materials with the model parameters obtained from existent static and ballistic experiments covering a wide range of strains, strain rates, and pressures. They performed computations to demonstrate the ability of the model to capture the material response under a broad range of experimental conditions including conditions out of those used to generate the parameters.

The validity of the AlN constitutive model of Holmquist et al. (2000b, 2001) was additionally tested, investigating the effects of ceramic layering configurations on ballistic performance (Holmquist et al., 2000a). The performance of the ceramic barrier was evaluated as a function of the number of ceramic layers, bonding the layers and the type of support used. The results, consistent with experiments, showed that ballistic performance is improved reducing the number of ceramic layers and the monolithic configuration has the best performance. The reason for that was demonstrated to be the tensile damage that initiates in the rear surface of each layer. Performance improvements were also noticed when the layers were bonded together. The bonding couples the shear strength across boundaries increasing the overall stiffness and the ballistic performance.

An advanced constitutive model of AlN exhibiting a first-order phase transition was proposed by Holmquist et al. (2000c). AlN has an SPT from the wurtzite to the rocksalt structure under high hydrostatic pressure or with high strain rate shock wave loading. The model suitable to describe phase changes in materials was initially used for crushable materials and adjusted in the study for AlN, modeling the phase change in the pressure–volume relationship, reflecting the 20% volume loss during the SPT. The pressure–volume response for AlN included both the wurtzite and rocksalt phase and was matched to experimental data. A simulation of plate impact provided a wave profile and pressure–volume consistent with experiments.

## 2.3. Atomistic simulations of projectile impact

Atomistic simulation approaches based on the MD method circumvent most of the restrictions of the FEM by directly dealing with the microscopic features of the system under study. Using reliable interatomic potentials, material properties such as symmetries, interface interactions, nonlinear and/or plastic deformation responses can be studied by the MD scheme. The main limitation of the MD approach is the limited number of atoms that can be simulated, which is directly proportional to the computational power available. Usually, nanoscale systems are simulated and no direct comparison with experiments is possible. In spite of that, MD simulations have proven to be a powerful tool to the understanding of the microscopic sources of damage initiation and development. Few studies attempted to capture the microscopic mechanisms of damage during a projectile impact, even though many MD simulations were performed to understand the effects of shock in materials. Below some of the MD studies of shock phenomena and some of the few simulations of projectile impacts on materials are discussed.

The MD simulation of shock waves started to get attention with the early simulations of Holian, Straub and collaborators. A three-dimensional (3D) simulation of shock waves in a perfect fcc crystal at nonzero temperature performed by Holian and Straub (Holian and Straub, 1979) using a Lennard-Jones potential showed that shock wave propagation have a transition from linear growth of the shock wave thickness (nonsteady wave) to a finite shock wave width (steady wave) as the shock strength is increased. They related the transition to the increase in coupling between vibrational excitations normal and transverse to the direction of the shock wave propagation. The result showing the steady state nature of shock wave propagation in finite temperature crystals prove the validity of the Rankine–Hugoniot jump conditions to planar shock waves, as the MD simulations explicitly obey the conservation laws. A comparison of nonequilibrium MD simulations and the Navier–Stokes (NS) continuum mechanics description of shock waves was studied by Holian et al. (1980). The shock waves were simulated using a Lennard–Jones fluid with uniaxial shrinking periodic boundary conditions. The profiles of stress, energy, and temperature of a strong steady dense-fluid shock wave simulated using 4800 atoms was compared with the NS derived profiles showing little differences. Holian (1988) performed yet a shock wave study using Lennard–Jones crystals showing that

shear stress relaxation in these materials is achieved through atomic rearrangement behind the shock front. In the case of fluids, the shear stress relaxes by transverse motion in a viscous way. For strong shock wave in solids the shear–stress relaxation is achieved by plastic flow highly localized in the shock front, involving slippage along close-packed planes. For shocks of intermediate strength, the shock wave exhibit an elastic precursor running out in front of the steady plastic wave, where slippage similar in character to that in strong shock waves relax the shear stress. For weak shock waves only elastic compression with no permanent transverse atomic strain is developed.

The ability of MD simulations to model the propagation of shock waves in energetic materials was demonstrated by Brenner et al. (1993), simulating a chemical detonation of a 2D solid. They used a reactive many-body potential to model an energetic material and showed that the chemically sustained shock wave has features consistent with experiments and the classical continuum theory of planar detonations. Based on 2D MD simulations using Tersoff-type potentials, Robertson et al. demonstrated the generation and evolution of split shock waves resulting from a dissipative polymorphic transition. The shock wave induced driven piston in the 2D solid, made of 5000 atoms, exhibits both single and split shock waves depending on the piston velocity. The results in excellent agreement with continuum theory showed that the transition accompanied by a large volume change is consistent with the Rankine–Hugoniot equations.

Recently, Holian and Lomdahl (1998) used large-scale MD simulations to demonstrate that fcc metals slip along all {1 1 1} slip planes, in different places along the shock front. The large 3D crystal used in the simulation eliminated the possibility that the observed slippage was an artifact of the transverse periodic boundary conditions. The mechanisms responsible for the nucleation of defects leading to plastic flow in perfect fcc single crystal was also investigated by Tanguy et al. (2003). They used nonequilibrium MD simulations with Lennard–Jones atoms to study the glide in ⟨1 0 0⟩ aligned fcc crystals. It was shown that shear stress is released by nucleation of small dislocation loops from thermal fluctuations behind the shock front, in a narrow region of a few lattice parameters.

Microscopic mechanisms of shock-induced SPT on a large-scale iron system were investigated by Kadau et al. (2002) using large-scale MD simulations. Depending on the strength of the shock wave (velocity of the piston) three regimes are generated. For low piston velocity only elastic compression of the system is achieved. Above a critical velocity, homogeneous nucleation of hcp grains nucleate in the shock compressed bcc crystal growing on a picosecond time scale to form larger grains. An elastic precursor wave travels ahead of this transformation wave. For strong shock waves an overdriven transformation wave develops and drives the intact bcc crystal directly into the hcp phase with no presence of an elastic precursor wave.

New MD methodology was also proposed to study shock waves within the MD scheme using thermodynamic constraints on the computational cell (Maillet et al., 2001a; Ravelo et al., 2004; Reed et al., 2003a, 2006; Zhakhovskii et al., 1999). These methods use a smaller cell compared to nonequilibrium simulation and focus only on the thermodynamic jump conditions across the shock wave. Zhakhovskii et al. (1999) introduced a computational cell which moves at the shock speed. That simulates a continuous pseudoinfinite system, by introducing and removing atoms on the boundaries along the propagation of the shock wave keeping it fixed in the center of the total system. The constant-volume uniaxial Hugoniostat, proposed by Maillet et al. (2001b) and its extension, the constant-stress proposed by Ravelo et al. (2004) were shown to easily identify phase transitions along the shock states and multiple wave structures agreeing well with standard nonequilibrium MD. A numerical methodology to study single and double shock waves was developed by Reed et al. (2003b, 2006), combining the MD method and Euler equations for compressible flow. The main advantage of the proposed method is that it enables the MD simulation of a system under dynamical shock conditions for longer periods of time than it is possible using nonequilibrium MD.

Hypervelocity impact simulations of a spherical cluster of 683 Lennard–Jones atoms on a rectangular plate composed of 8000 atoms was studied using MD simulations by Holian (1987). The ratio of the sphere diameter to the plate thickness and the velocity of the spherical cluster were chosen to match those of an experiment and a continuum simulation of a lead ball striking and penetrating a lead wall. The MD results showed considerable similarities in the debris cloud shape and distribution of mass per unit area. However, the MD, as well as the continuum simulations, shows dense regions in the middle of the debris cloud that does not resemble the experimental results. Holian argued that this is expected as the small length scale in MD favors the clustering of atoms during the debris-cloud expansion. Another MD simulation of hypervelocity impact

was performed by Mcdonald et al. (1993) to study the hole size formation on thin aluminum films. The film with 9216 atoms was impacted using two projectiles with 256 atoms and 512 atoms. The results on time evolution of density, pressure, and temperature for impacts at 7, 9 and 11 km/s show that the results are consistent with experimental curves but apparently underestimate experimental values with exception of the calculated pressure. The hole sizes predicted by MD, after a scaling element is used, are significantly smaller than those found using a continuum hydrodynamic simulations. The authors emphasize the need of using more realistic potentials for metals and the need of large-scale simulations to effectively model hypervelocity impacts.

## 3. Methodology for large-scale molecular dynamics simulations of impact

### 3.1. Interatomic potential model

#### 3.1.1. Description of the model

The interaction potential model encodes interactions among all the atoms and therefore is a critical ingredient of an MD simulation. Our interatomic potential of AlN is based on the interatomic potential model developed by Vashishta et al. (1990) to describe semiconductors and ceramic materials. The functional form of the potential consists of two- and three-body terms,

$$U = \sum_{i<j}^{N} U_{ij}^{(2)}(r_{ij}) + \sum_{\substack{i,j<k \\ j \neq i, k \neq i}}^{N} U_{jik}^{(3)}(\vec{r}_{ij}, \vec{r}_{ik}), \tag{1}$$

where $N$ is the number of atoms, $r_{ij} = |\vec{r}_{ij}|, \vec{r}_{ij} = \vec{r}_i - \vec{r}_j$, and $\vec{r}_i$ is the position of the $i$th atom.

The two-body term represents various physical effects such as the steric repulsion, Coulomb interaction due to charge transfer, induced charge–dipole interaction due to large electronic polarizability of the anions and van der Waals (induced dipole–dipole) interaction:

$$U_{ij}^{(2)}(r) = \frac{H_{ij}}{r^{n_{ij}}} + \frac{Z_i Z_j}{r} e^{-r/r_{1s}} - \frac{D_{ij}}{r^4} e^{-r/r_{4s}} - \frac{w_{ij}}{r^6}, \tag{2}$$

where $H_{ij}$ and $n_{ij}$ are the strength and exponent of the steric repulsion, $Z_i$ the effective charge, $D_{ij} = 1/2(\alpha_i Z_j^2 + \alpha_j Z_i^2)$ the strength of the charge–dipole interaction with $\alpha_i$ the electronic polarizability, $r_{1s}$ and $r_{4s}$ are the screening constants for the Coulomb and charge–dipole interactions, and $w_{ij}$ the strength of the van der Waals interaction. The three-body term represents covalent bond bending and stretching:

$$U_{jik}^{(3)}(\vec{r}_{ij}, \vec{r}_{ik}) = B_{jik} \exp\left(\frac{\xi}{r_{ij} - r_0} + \frac{\xi}{r_{ik} - r_0}\right) \frac{(\cos \theta_{jik} - \cos \theta_0)^2}{1 + C_{jik}(\cos \theta_{jik} - \cos \theta_0)^2}, \quad (r_{ij}, r_{ik} \leq r_0), \tag{3}$$

where $B_{jik}$ is the strength of the three-body interaction, $r_0$ the cut-off radius, $\xi$ and $C_{jik}$ constants to adjust the stretching and bending terms, and $\theta_{jik}$ the angle formed by $\vec{r}_{ij}$ and $\vec{r}_{ik}$. $\theta_0$ in the case of AlN is the tetrahedral angle 109.5°, with $\cos \theta_0 = -1/3$. This interaction potential model was successfully used to study a number of ceramic materials such as $SiO_2$ (Campbell et al., 1999; Vashishta et al., 1990), $Si_3N_4$ (Kalia et al., 1997a, b; Tsuruta et al., 1998; Vashishta et al., 1995; Walsh et al., 2000), and SiC (Chatterjee et al., 2000; Shimojo et al., 2000; Szlufarska et al., 2005).

#### 3.1.2. Validation of potential parameters

In the present work, we use this model with the parameters optimized to reproduce a selected experimental data for AlN. Our fitting database includes crystalline lattice constants, cohesive energies, elastic constants (Iwanaga et al., 2000), and melting temperature. The potential parameters are given in Table 1. The calculated elastic constants and sound velocities are given in Table 2.

An SPT is expected under impact, and should be described by the interatomic potential. Fig. 1 shows the energetics of the wurtzite and rocksalt phases and the phase transition pressure, 25 GPa, calculated from the common tangent of the two curves, which has a good agreement with the experimental values reported to be in the range 12.5–22.9 GPa for bulk systems (Christensen and Gorczyca, 1993; Gorczyca et al., 1991; Kipp and

Table 1
Parameters in the interaction potential for AlN

|  | $Z$ (e) | | | | $\alpha$ (Å$^3$) |
|---|---|---|---|---|---|
| Al | 1.0366 | | | | 0.0 |
| N | −1.0366 | | | | 3.0 |

|  | $H$ (J Å$^\eta$) | $\eta$ | $W$ (J Å$^6$) | $r_{1s}$ (Å) | $r_{4s}$ (Å) |
|---|---|---|---|---|---|
| Al–Al | $8.7162 \times 10^{-17}$ | 7.0 | 0.0 | 5.0 | 3.75 |
| Al–N | $2.6824 \times 10^{-18}$ | 9.0 | $9.7901 \times 10^{-18}$ | 5.0 | 3.75 |
| N–N | $2.1790 \times 10^{-17}$ | 7.0 | 0.0 | 5.0 | 3.75 |

|  | $B$ (J) | $C$ | $\xi$ (Å) | $r_0$ (Å) | $\theta$ |
|---|---|---|---|---|---|
| Al–N–Al | $40 \times 10^{-19}$ | 30.0 | 1.0 | 2.6 | 109.47122 |
| N–Al–N | $40 \times 10^{-19}$ | 30.0 | 1.0 | 2.6 | 109.47122 |

Length and energy units are Angstroms (Å) and Joules (J), respectively. $Z$ is the effective charge in units of electron charge, $e$, and $\alpha$ is the electronic polarizability, in units of Å$^3$; $H$ is the repulsive strength; $\eta$ repulsive exponents; $w$ the van der Waals strength; and $r_{1s}$ and $r_{4s}$ are the screening constants. The other parameters in the three-body interaction potential are defined by the three-body potential equation.

Table 2
Elastic constants and sound velocities of AlN calculated from the interatomic potential model compared to experimental values

| Elastic constants | $C_{11}$ | $C_{12}$ | $C_{13}$ | $C_{33}$ | $C_{44}$ | Bulk modulus |
|---|---|---|---|---|---|---|
| Exp.[a](GPa) | 411 | 149 | 99 | 389 | 125 | 211 |
| Model (GPa) | 371 | 126 | 116 | 452 | 119 | 211 |

| Direction of propagation | Direction of displacement | Type of wave | Velocity expression | Exp.[a] (km/s) | Model (km/s) |
|---|---|---|---|---|---|
| $\langle 0\,0\,1 \rangle$ | $\langle 0\,0\,1 \rangle$ | Longitudinal | $\sqrt{C_{33}/\rho}$ | 10.97 | 11.82 |
| $\langle 0\,0\,1 \rangle$ | $\langle 1\,0\,0 \rangle$ or $\langle 0\,1\,0 \rangle$ | Transverse | $\sqrt{C_{44}/\rho}$ | 6.22 | 6.06 |
| $\langle 1\,0\,0 \rangle$ | $\langle 1\,0\,0 \rangle$ | Longitudinal | $\sqrt{C_{11}/\rho}$ | 11.27 | 10.71 |
| $\langle 1\,0\,0 \rangle$ | $\langle 0\,1\,0 \rangle$ | Transverse | $\sqrt{(C_{11} - C_{12})/(2\rho)}$ | 6.36 | 6.15 |
| $\langle 1\,0\,0 \rangle$ | $\langle 0\,0\,1 \rangle$ | Transverse | $\sqrt{C_{44}/\rho}$ | 6.22 | 6.06 |

Sound velocities were calculated with $\rho = 3.2353 \, \text{g/cm}^3$.
[a] Iwanaga et al. (2000).

Grady, 1994; Mashimo et al., 1999; Uehara et al., 1997; Ueno et al., 1992; Xia et al., 1993). Recently, two studies indicated the transformation pressure could depend strongly on the surface to volume ratio for nanocrystals (Wang et al., 2004) and nanowires (Shen et al., 2006).

The energy barrier for plastic deformations is estimated by calculating the generalized stacking fault energy in the basal plane of the wurtzite AlN by both MD and *ab initio* quantum mechanical calculations based on the density functional theory (DFT) (Hohenberg and Kohn, 1964; Kohn and Vashishta, 1983). The electronic-structure calculations are based on the generalized gradient approximation (Perdew et al., 1996) for the exchange-correlation energy (Cohen, 1993; Hohenberg and Kohn, 1964; Ogata et al., 2001). The ultrasoft pseudopotential (Vanderbilt, 1990) is employed for the interaction between the valence electrons and ions. The electronic wave functions are expanded by the plane-wave basis set. The energy functional is minimized using an iterative scheme based on the preconditioned conjugate-gradient method (Kresse and Hafner, 1994; Ogata et al., 2001) with a sufficient k-point sampling in the first Brillouin zone.

The calculation procedure of the generalized stacking fault energy follows that of Tadmor and Hai (2003) adapted for the wurtzite crystal structure. An AlN bulk single crystal sample with 20 atomic layers in the
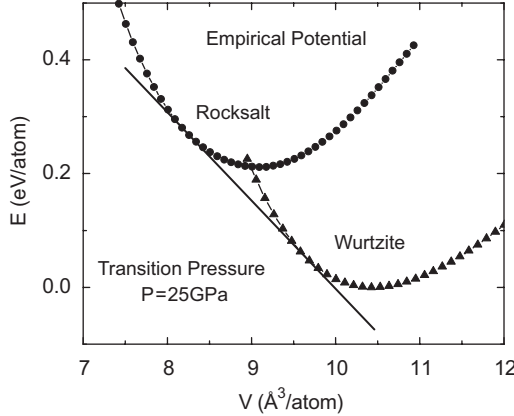
Fig. 1. Energy–volume relations for the crystalline AlN calculated using the present interatomic potential. Triangles correspond to the wurtzite structure, while circles correspond to the rocksalt structure. The 25 GPa structural transition pressure, estimated from the common tangential line of the wurtzite and rocksalt curves, is compatible with the range of experimental transformation pressures.

[0 0 0 1] direction was setup (see Fig. 2(a). A set of 15 layers was rigidly slid in the $1/3[1\,0\,\bar{1}\,0]$ direction using a 30 small steps forming two parallel intrinsic stacking fault type I (Dovidenko et al., 1997; Stampfl and Van de Walle, 1998; Wright, 1997). The atomic configurations were relaxed, performing a quench to $T = 0$ K, for 5000 steps in the [0 0 0 1] perpendicular after each step of the sliding, in order to obtain a minimum energy configuration. Thirteen layers inside the initial 15 are additionally slid in the $-1/3[1\,0\,\bar{1}\,0]$ direction to get two parallel micro twins (a basic unit in a twin deformation process). Fig. 2(a) shows the configurations at the beginning, when the stacking fault is created and when the micro-twin is completed. The energetics of the rigid sliding shows good agreement between MD and DFT results. The value of the unstable stacking fault energy (first peak) is 133 meV/Å² (MD) and 147 meV/Å² (DFT), the unstable twinning energy is 130 meV/Å² (MD) and 152 meV/Å² (DFT).

### 3.1.3. The projectile and its interaction with the target

Experimentally, the best projectiles available are armor piercing bullets with a high hardness steel or tungsten carbide core. We used a projectile with heavy mass (five times that of AlN target) and high hardness (five times that of AlN), making it a high performance armor piercing projectile which is able to overcome the rigid barrier posed by the AlN ceramic and cause extensive damage.

The forces between atoms in the projectile are calculated using the same interaction potential of the AlN target with parameters scaled to make the projectile five times stiffer than the target. The forces between atoms in the projectile and target were calculated using an average of the repulsive part of the target and projectile potentials.

### 3.2. Parallel molecular dynamics method

In the MD approach, one obtains the phase-space trajectories, i.e. the time evolution of the positions and momenta for all the atoms from the numerical solution of the Newton's equations of motion (Allen and Tildesley, 1990),

$$m_i \frac{\mathrm{d}^2}{\mathrm{d}t^2} \vec{r}_i = -\frac{\partial}{\partial \vec{r}} U \quad (i = 1, \ldots, N), \tag{4}$$

where $m_i$ is the mass of the $i$th atom, $N$ is the number of atoms, and $U$ is the potential function.

Eq. (4) is integrated by discretizing time with an interval, $\Delta t$, and applying a finite-difference integrator that depends on the statistical ensemble used. In this study while the simulation is done out of equilibrium the number of atoms, $N$, the system volume, $V$, and the total energy, $E$ are conserved quantities, which corresponds to the use of the microcanonical ($NVE$) ensemble. To integrate the MD equations of motion, the
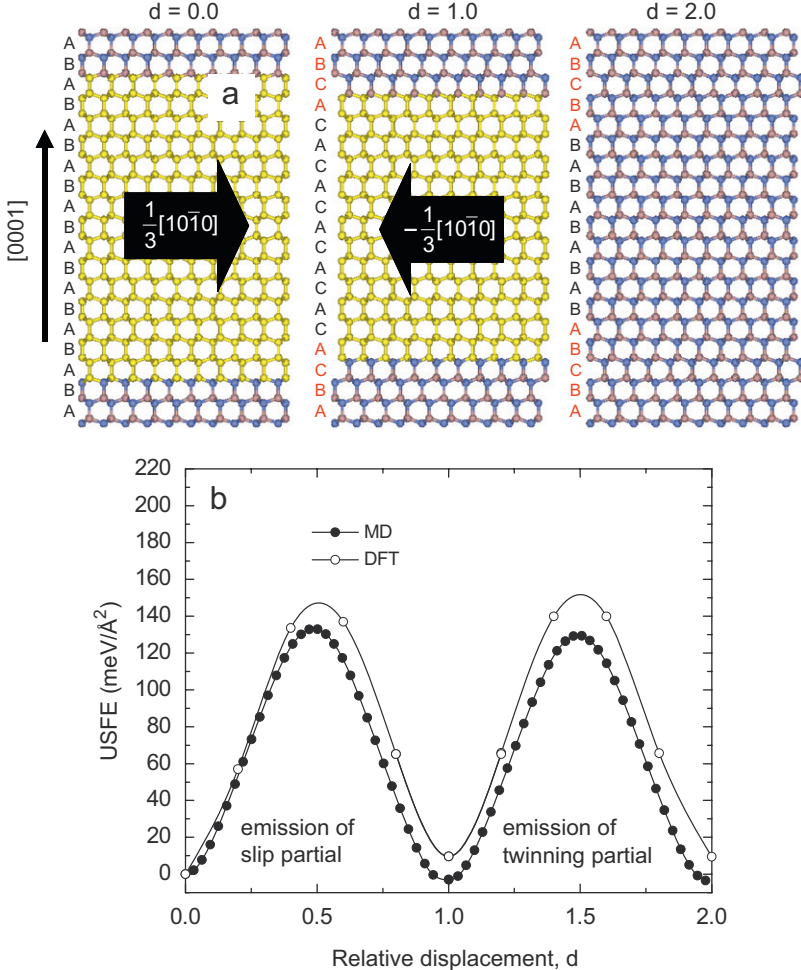
Fig. 2. Calculation of the generalized stacking fault energy curves for AlN wurtzite using the interatomic potential model and DFT. (a) Shows the crystal system used for the rigid slipping projected along the [1 1 $\bar{2}$ 0] direction. The left panel in (a) shows the perfect ABAB wurtzite structure packing, with relative displacement $d = 0.0$, with the atoms to be used in the slipping in yellow. The central panel in (a) shows the system with a pair os stacking faults at relative displacement $d = 1.0$, with the atoms to be used in the twinning in yellow. The right panel of (a) shows the system with a pair of microtwins ABCBA. (b) Shows the energetics for the slipping and twinning using both the potential model and DFT. For both methods, the potential energy for rigid glide slipping along the partial dislocation direction (relative displacement, d, between 0 and 1), resulting in a stacking fault type I, is calculated as well as along the potential energy curve for slip with a subsequent twinning partial, resulting in a microtwin. The first energy maximum corresponds to the unstable stacking fault energy, while the second maximum corresponds to the unstable twinning energy. The middle minimum, $d = 1.0$, corresponds to the stacking fault energy.

velocity-Verlet algorithm is used with a time step of 1.5 fs that conserves the energy at least to the third meaningful digit during the whole simulation.

### 3.2.1. System setup

The simulated ceramic target is an AlN monocrystal slab 100.4 nm thick in the impact ($z$) direction, and 146.6 nm × 149.4 nm wide in the lateral ($x$ and $y$) directions, involving 208,896,000 atoms (see Fig. 3). The [0 0 0 1] direction of the wurtzite crystal structure of AlN is aligned with the $z$-direction, while $x$ and $y$ are aligned along [1 $\bar{1}$ 0 0] and [1 $\bar{2}$ 0 0] directions. To minimize edge and surface effects, periodic boundary conditions are applied in the $x$ and $y$ directions while in the impact direction the target has two free surfaces. The projectile is a wurtzite monocrystal with 550,656 atoms in a hexagonal cylinder shape, 15 nm wide and 30 nm long. The crystal orientations of the projectile are the same as the target.
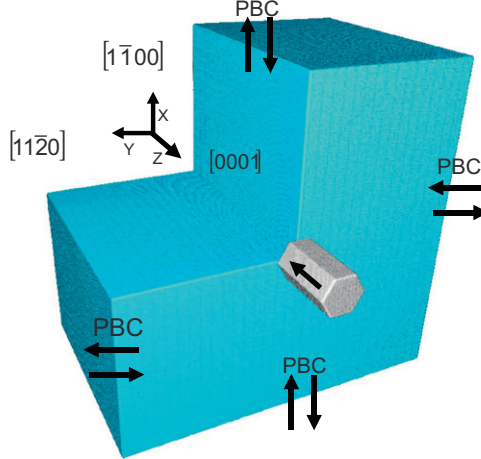
Fig. 3. Setup of the impact simulation, showing the prismatic target in a three-quarter view and the hexagonal cylinder projectile. The impact is done against the [0 0 0 1] direction of the AlN wurtzite target. Periodic boundary conditions (PBC) are applied in the $x$ and $y$ directions perpendicular to the impact in the $z$-direction. The target with 208 million atoms is 1000 Å long in the $z$-direction and $1500 \times 1500$ Å wide in the $x$- and $y$-directions. The hexagonal cylinder projectile with 500,000 atoms is 300 Å long and 150 Å wide and has the same crystal orientations of the target.

The initial system is setup using the following steps:

 (i) A bulk AlN wurtzite crystal enclosing the target and projectile volumes was generated;
 (ii) The target and projectile bodies were defined eliminating the excessive atoms from the original system using a set of predefined planes in space. These planes were precisely adjusted to not allow dangling bonds (one-coordinated atoms) on the projectile or target surfaces avoiding surface instabilities. This is the reason for the choice of a hexagonal-shaped projectile, as the wurtzite structure has hexagonal symmetry;
(iii) The atoms in the projectile body region are set at as projectile atoms and will have different properties than those in the target region;
(iv) The surfaces on the target and projectile are relaxed by quenching the entire system, consisting of 209,446,656 atoms, for 5000 time steps to 0 K (MD time step is 1.5 fs), and subsequently setting the temperature at 1 K using a Maxwell distribution of velocities. This step eliminates possible stress waves generated in the surface reconstruction process when the initial bulk system is molded.
 (v) 100 nm layers of vacuum are added on each side of the system in the $z$-direction.
(vi) A 15 km/s impact $z$ velocity is set for the projectile atoms.

After the system is setup, the simulation is performed in the microcanonical ensemble. The total simulation time is 31.5 ps (or 21,000 MD time steps), which is sufficient to track the full propagation of the shock wave since the projectile hit the center of the (0 0 0 1) free surface of the target until the shock wave cross the entire system and generates a reflected tensile wave allowing the nucleation of damage, leading to crack propagation.

### 3.2.2. Spatial decomposition

The MD simulations are performed for 500 hours on 512 Intel Xeon processors connected by Myrinet network. We use a spatial decomposition scheme (Rapaport, 1991) and a six-step message passing algorithm. To have a balanced load among processors, the total system is two dimensionally decomposed into a $16 \times 32$ by one array in the $x$-, $y$-, and $z$-direction, i.e. the physical system is simulated using 16 processors in the $x$, 32 processors in the $y$, and 1 processor in the $z$-direction. Therefore, each of the processor simulates 1/512 of the total system in the $xy$ plane along all $z$. This decomposition achieves a reasonable balanced load among processors as the impact simulation develops and the target and projectile deformation and flow arises. The MD code is written in Fortran with MPI (message passing interface) for parallelization. The running time scales linearly with number of atoms using Myrinet network, which means running a 512 million atom

simulation on 512 nodes takes nearly the same as running a million atom simulation on a single node. Initially, each node simulates roughly a 400,000 atoms subsystem and the simulation runs at about 3000 steps a day. The average of about 30 s per time step comprises the calculation of the two- and three-body forces for each atom, the integration of the equations of motion, calculation of properties, and I/O of data to disk. In this large-scale simulation, the I/O is kept local, i.e. each node saves the information of each subsystem in a local disk. This is important since network communication could fail if all nodes write onto the same disk. The files from 512 nodes are concatenated for analysis after the simulation is complete.

### 3.3. Calculation of properties

#### 3.3.1. Correlation functions

Correlation functions are calculated during the simulation to analyze the regions of structural transformation. Radial distribution function, coordination numbers and bond–angle distribution are used to distinguish the low-pressure wurtzite phase from the higher pressure rocksalt phase of AlN. The total radial distribution function is defined as:

$$g(r) = \frac{V}{N} \frac{n(r)}{4\pi r^2}, \tag{5}$$

where $V$ is the volume, $N$ is the number of atoms and $n(r) = 1/N \langle \sum_{i \neq j=1}^{N} \delta(r - r_{ij}) \rangle$, where the brackets denotes the ensemble average. During the simulation a histogram is computed with the distances of neighbor atoms in the system, which is further used to compute $n(r)\Delta r$, the number of atoms between $r$ and $r + \Delta r$, and $g(r)$. The coordination number function defined by Eq. (6) gives the average number of neighbor atoms within a distance $R$,

$$N(R) = 4\pi \frac{N}{V} \int_0^R g(r) r^2 \, dr. \tag{6}$$

In this work, we define the coordination number of an atom as the number of neighbor atoms within $R = 2.5 \,\text{Å}$ at a given time. The value of $R$ is defined based on the minimum value of the $g(r)$ curve for the wurtzite phase of AlN, between the first and second peak. In the tetrahedral wurtzite structure, the atoms are four-fold coordinated, while they are six-fold coordinated in the cubic rocksalt structure. Transformed atoms are searched during the simulation selecting the six-coordinated atoms. Pair correlation function and bond angle is further calculated to ensure that the selected six-coordinated atoms are in fact in the rocksalt structure and not just in highly compressed regions.

The bond–angle distribution is a three-body correlation function. To calculate bond–angle distributions in the MD simulation we use the same cutoff distance of $R = 2.5 \,\text{Å}$ to define the nearest-neighbor list for each atom. In a two-component system with species $A$ and $X$, the set of possible bond–angle distributions to consider is {$X–A–X$, $A–X–A$, $A–A–X$, $X–X–A$, $A–A–A$, $X–X–X$}. However, for the purpose of this simulation it is sufficient to analyze the Al–N–Al and N–Al–N correlations. From the nearest-neighbor list for each $A$ atom, a histogram is constructed from all $X–A–X$ angles. The bond–angle distributions for the wurtzite and rocksalt phases of AlN are very different and can be used to delineate the phases. The four-coordinated wurtzite bond–angle distribution has a single peak at the angle of 109.5° from the tetrahedral bonding, while the six-coordinated rocksalt bond–angle distribution has two peaks at angles 90° and 180°.

#### 3.3.2. Local stress distribution

After the impact, both temperature and pressure become extremely high, and strong gradients are formed in the system during the rise time of the shock wave. To characterize the generation and development of the shock wave, we calculate pressure and stresses based on appropriately averaged local virial values as a function of time. The viral expression of the stress tensor is given by

$$V\sigma_{\alpha\beta} = \sum_i m_i v_\alpha^i v_\beta^i + \frac{1}{2} \sum_i \sum_{j \neq i} \left( -\frac{1}{r} \frac{\partial U}{\partial r} \right) r_\alpha r_\beta |_{r=r_{ij}}, \tag{7}$$

where $V$ is the volume of the system, $\alpha$ and $\beta$ are the Cartesian $xyz$ components, $\sigma_{\alpha\beta}$ is one of the nine components of the stress tensor, $\mathbf{v}^i$ and $\mathbf{r}^i$ are the velocity and position vectors of atom $i$, and $U$ is the interatomic potential function. Eq. (7) provides a standard way to calculate stresses in MD simulations of bulk system at equilibrium. However, it is not straightforward to apply it if surfaces, inhomogeneities, and stress gradients are present or if the system is out of equilibrium. To deal with these conditions, several approaches have been developed to calculate the stress distribution with reasonable physical meaning (Cheung and Yip, 1991; Cormier et al., 2001; Lutsko, 1988; Nakane et al., 2000; Todd et al., 1995; Tsai, 1979). Unfortunately, none of these approaches is suitable to calculate the local stress distributions generated by shock waves in binary materials like AlN. To overcome this restriction, we use an alternative definition of the stress tensor that is convenient to describe the atomic level stress distribution of shock waves in multicomponent systems, like AlN, while still consistent with the bulk ensemble average values.

Starting from Eq. (7) for each atom inside the volume $V$ we have

$$\sigma_{\alpha\beta}^i = m_i v_\alpha^i v_\beta^i + \frac{1}{2} \sum_{j \neq i} \left( -\frac{1}{r} \frac{\partial U}{\partial r} \right) r_\alpha r_\beta |_{r=r_{ij}}, \tag{8}$$

where the summation in the second term on the right side is over all the atoms inside the range of the interatomic potential $U$. To calculate the stress bulk average, the atomic contributions to the virial given by Eq. (8) are averaged inside the total system volume $V$ recovering Eq. (7)

$$V\sigma_{\alpha\beta} = \sum_i \sigma_{\alpha\beta}^i. \tag{9}$$

The local stress distribution is calculated from contributions inside a local volume with nanoscale dimensions. A natural way to define this local volume is equally dividing the system into small cubic voxels (volume pixels). The stresses averaged in each of these voxels will provide a grid with the local stress distribution in the total system. This approach was used successfully in large-scale MD simulations of stress relaxation at materials interface (Bachlechner et al., 1998; Omeltchenko et al., 2000). Although this choice of voxel is convenient for problems of stress relaxation in stable solids, it is not a good choice for the description of strong shock waves with large gradients of stress and flux of atoms. We choose instead to calculate the local stresses in the distribution grid using spherical voxels. Around each point of the grid, the atomic contributions of atoms inside a spherical volume centered at the grid point are averaged. This provides a smoother average of the local stress, especially close to the shock wave front. Instead of using a grid of equally spaced points in space to represent the stress distribution, one can alternatively use the position of the atoms themselves as nonuniform grid points. The dynamics of the atoms and the damage mechanisms can be tracked while the
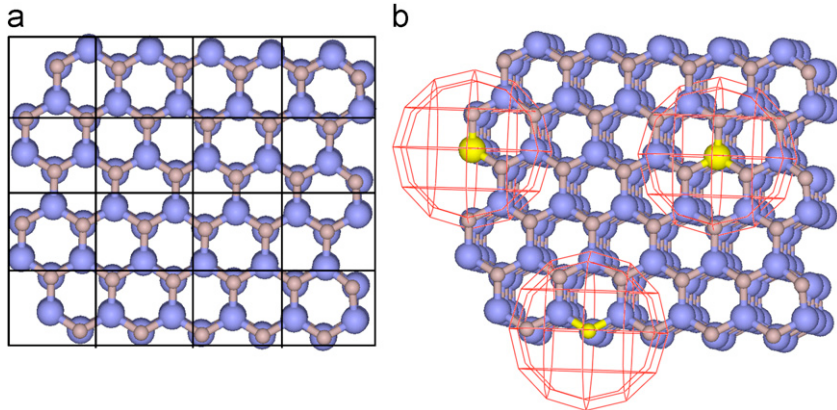


Fig. 4. Choices of voxels to calculate the local stress distributions. (a) Shows the prismatic voxels where the total simulation volume is divided in nanoscale cubic volumes where the stress is averaged. (a) Provides the local distribution of stress in the form of an equaly spaced grid in space. (b) Shows the spherical voxels centered on each atom in the structure where the stress is averaged. (b) Provides the local distribution of stress in the position of each atom in the structure. The spherical voxels shown in (b) with the sphere radius conveniently adjusted is a better choice than (a) to describe the local stress on shock waves, close to defects and surfaces.
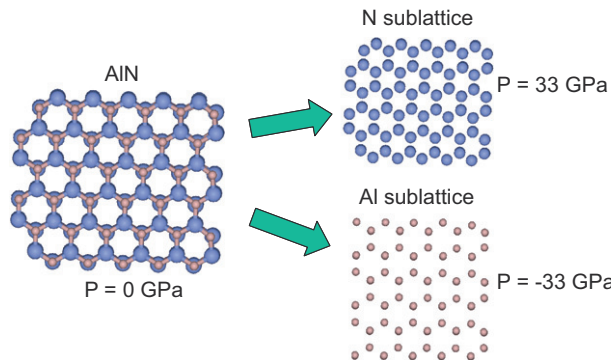
Fig. 5. Stresses in the AlN structure. For the AlN structure at hydrostatic pressure $P = 0$ GPa its N and Al sublattices experience very different pressures. Using the proposed interatomic potential, the hydrostatic pressure averaged on only the N sublattice is $P = 33$ GPa, while it is $P = -33$ GPa for the Al sublattice.

local stress distribution in the region around each atom is dynamically monitored. Fig. 4 shows the spherical choice of voxels for the AlN wurtzite crystal. The radius of the spherical voxel defines how large is the volume where the stress is averaged and also defines the resolution of the stress distribution. The larger the voxel less details will be available of any defects that can be possibly generated.

An important issue in the calculation of stress distribution in multicomponent system is the stoichiometry of the set of atoms inside each voxel. As shown in Fig. 5, the stresses in each sublattice in an alloy, such as AlN, can vary widely both in sign and magnitude, even if the total stress is zero. If the correct stoichiometry of the alloy is not represented inside the voxel the averaged stress will biased by the component in excess in the voxel. To avoid this problem we enforce stoichiometric average inside the voxel. Inside each voxel, the stress is calculated using the expression given by

$$\sigma_{\alpha\beta} = \frac{n_{\mathrm{Al}} + n_{\mathrm{N}}}{2w} \left[ \frac{1}{n_{\mathrm{Al}}} \sum_{i=1}^{n_{\mathrm{Al}}} \sigma_{\alpha\beta}^i \bigg|_{\mathrm{Al}} + \frac{1}{n_{\mathrm{N}}} \sum_{i=1}^{n_{\mathrm{N}}} \sigma_{\alpha\beta}^i \bigg|_{\mathrm{N}} \right], \tag{10}$$

where $n_{\mathrm{Al}}$ and $n_{\mathrm{N}}$ are the number of Al and N atoms inside and $w$ the volume of the voxel. The first summation is made on the Al atoms, while the second on the N atoms inside the voxels. If the number of Al and N are the same inside the voxels and therefore the stoichiometry is correct it is straightforward to show that Eq. (10) gives the virial average expression of Eq. (9) for $V = w$. For small voxels, the density given by $(n_{\mathrm{Al}} + n_{\mathrm{N}})/w$ may have large fluctuations depending on the choice of $w$. One procedure is to estimate the local density increasing $w$ and calculating the density inside the voxel until the fluctuation is within an acceptable range. If the density fluctuation along the system is not large, the bulk value of the density can be used as a good approximation for $(n_{\mathrm{Al}} + n_{\mathrm{N}})/w$ at each time step.

In this work, the stresses are calculated from Eq. (10), from atomic centered spherical voxels of radius 2.5 Å to provide a sufficient resolution and to identify the shock wave and structural defects. Averages of these values over appropriate time and space are equivalent to experimentally measured values.

### 3.3.3. Identification of dislocations and nanocavities with ring statistics

The search for defects in large-scale datasets can be performed in several ways. Atoms in the core or around defects have different properties and that can be used as a criterion to identify and characterize defects in the system. Dislocations, for example, can be identified by the change in energy and coordination number associated with bond breaking. Nanocavities can be identified by the change in the local density as well as fracture surfaces. More accurate criteria for crystal defects identification can be established based on changes in the crystal topology. In this work, we use such a criterion based on the analysis of the shortest-path ring statistics for the AlN wurtzite topology.

Shortest-path ring statistics have long been used to characterize amorphous systems (Deleeuw et al., 1985; Ebbsjo et al., 2000; Franzblau, 1991; Guttman, 1990; Rino et al., 1993, 2004). The amorphous structure is
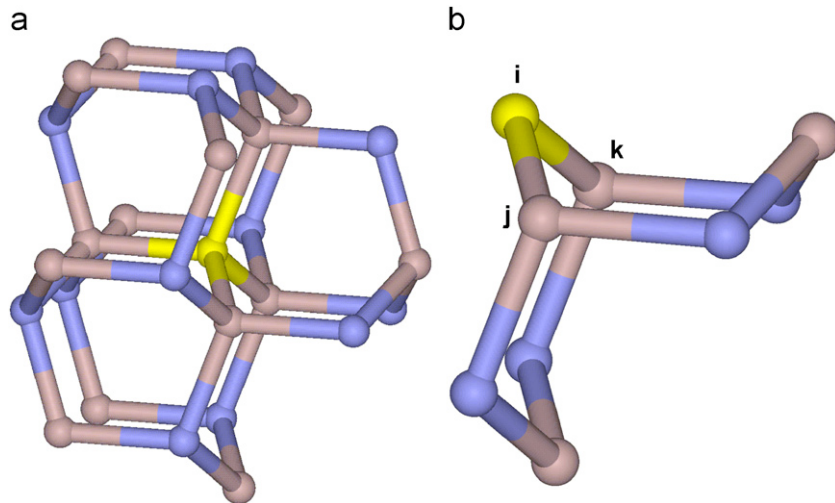
Fig. 6. Extracts from a perfect AlN wurtzite structure showing shortest-path rings. (a) Shows all the shortest-path rings that can be closed from one atom in the wurtzite structure, here the centered atom in yellow color. In the nondefective wurtzite structure, each atom has 12 shortest-path rings with 6 members, like the one showed in (a). (b) Shows the two possible six-member rings that can be closed from any two *jk* neighbors of an atom *i*. The search for rings in the structure is done considering all atoms in the structure as *i* and looking for the shortest path in the structure that connects neighbors atoms *j* and *k*.

difficult to characterize because it has no long-range order. Bond length, bond angle, and coordination number can provide information on the short-range order while ring statistics analysis is a useful technique to characterize the intermediate range order. The ring analysis can also be a very useful tool to readily identify crystalline structure defects as it is sensitive to small changes in the crystalline topology.

A shortest-path ring in the AlN crystal is defined as the shortest closed path of alternating Al–N atomic bonds. In a perfect AlN wurtzite structure, all the atoms have 12 shortest-path rings with six member atoms in each ring as shown in Fig. 6(a). From each pair of first neighbors in the wurtzite tetrahedral topology, two shortest-path rings with six members can be formed, and taking in account all the six possible pair of neighbors there are 12 rings with six members. Close to any defect, the size of the shortest-path rings will change as well as the number of six member rings per atom, which is used to identify and characterize them. Atoms on crack surfaces and on the surface of nanovoids will have half the number of rings per atoms in the bulk. For atoms in the core or immediately close to dislocations, the number of six member rings per atom will also be lower and that is used to select these atoms for further analysis.

The algorithm we use to calculate the shortest-path ring statistics (Zhang et al., 2006) is a version of the breadth-first search algorithm (Goldfarb et al., 1991). As in a standard graph problem, the search for rings in the structure requires two sets of data, the vertices—in our case the position of atoms—and the edges—in our case bonds connecting neighbor atoms. The position of the atoms is always available in MD while the bonds between atoms can be defined in several ways. In our work we define the bonds based on an interatomic distance criterion. Two atoms in the AlN structure are considered to have a bond if their position in space is distant from each other up to 2.5 Å. From the set of positions and bonds, the search for rings is done sequentially from the position of each atom *i* (Fig. 6(b)). The pairs of *jk* first neighbors of *i* are taken one by one and fixing *k* the connectivity path from atom *j* is extended by one bond level at a time in the structure following all possible interatomic bonds in the structure till atom *k* is reached and the path is closed.

## 3.4. Visualization techniques

The data in this work is visualized with the atomsviewer software (Sharma et al., 2003a, 2004; Sharma et al., 2003b), which is based on OpenGL and CAVE libraries. Atomsviewer was developed to handle billion-atom data sets and interactively visualize the data in 3D at nearly real-time.
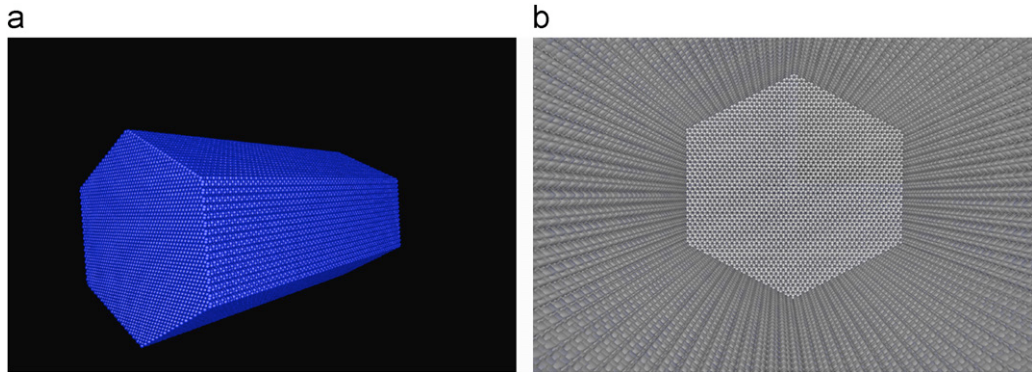
Fig. 7. Details of the projectile. (a) The hexagonal cylinder projectile with exactly 550,656 atoms is 300 Å long and 150 Å wide and has the same wurtzite structure of the target. (b) Shows that inside bulk atoms of projectile were removed to help reduce the size of the files used in the visualization. There are 105,376 atoms in the projectile skin what reduces the total number of atoms by roughly 81% of the initial total number of atoms.
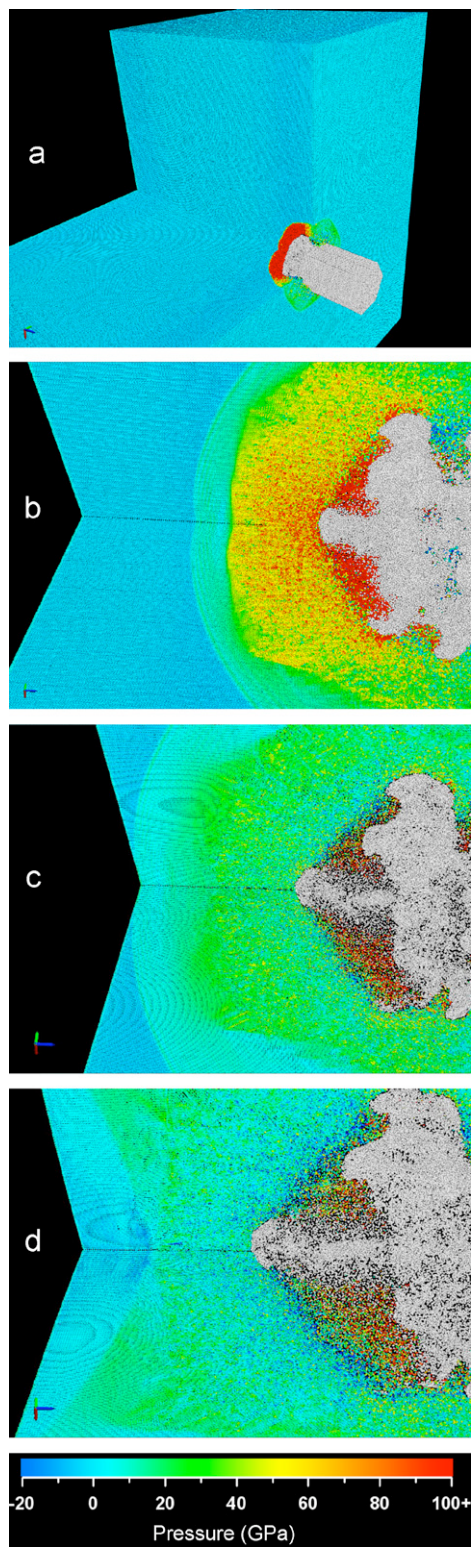
The main issue in the visualization and analysis of large-scale simulations is the time spent working with the huge amounts of data generated. This time includes the transfer of files, processing of data, analyzing and filtering data subsets of interest, generation of visualization files, and detailed 3D visualization. Each one of these steps may take weeks for a 200 million atoms simulation like the one performed in this work, depending on several factors such as network bandwidth, disk speed, CPU speed, BUS speed, and graphics card performance. The easiest way to minimize the time spent in the visualization process is to properly select interesting regions inside the total dataset that will be worth analyze and work only with this selected subset of data. In this work, usually no more than 10% of the 200 million atoms are needed to characterize the interesting phenomena at any time during the simulation. To make the data selection, several rules were applied to filter data during the simulation runtime and generation of files:

1. Planes of atoms 10 Å thick are setup in the $zx$ and $yz$ planes at the center of the system and all atoms inside them are selected. These planes of atoms, which are not selected based on its properties, are important to visualize the generation and development of the shock wave in the two perpendicular independents directions of the wurtzite crystal. Additionally, planes of atoms in the borders of the system are also selected. Fig. 3 shows the set of planes chosen.
2. Crystal defects are pre-selected using their coordination number. In the perfect AlN wurtzite structure, all the atoms have coordination 4. This coordination number is 6 for the rocksalt high-pressure phase of AlN and usually different from 4 around defects. In the selection of the atoms for visualization all the atoms with coordination 4 are eliminated. For a clearer visualization of the data atoms with coordination 5 are also eliminated.
3. The projectile in this simulation has roughly 500,000 atoms. As the projectile atoms properties are not important to this study only the atoms on its surface are selected to visualization. From the total 500,000 atoms more than 100,000 atoms are lying on the surface and are selected. Fig. 7(a) and (b) shows details of the shape and size of the projectile and the bulk atoms eliminated from the data set used in the visualization.
4. Ring analysis is used as a post-processing step performed on selected frames of data to accurately filter defects in the total system. Usually no more than 10% of the atoms are filtered using the ring analysis, which indicates that no more than 10% of the volume of the total system is seriously damaged.

## 4. Results

### 4.1. Shock wave generation

At the impact region, the projectile tip starts to rapidly compress the target surface, creating a local explosive scenario (see Fig. 8(a)). Because of the high 15 km/s impact velocity, the projectile initially releases a large amount
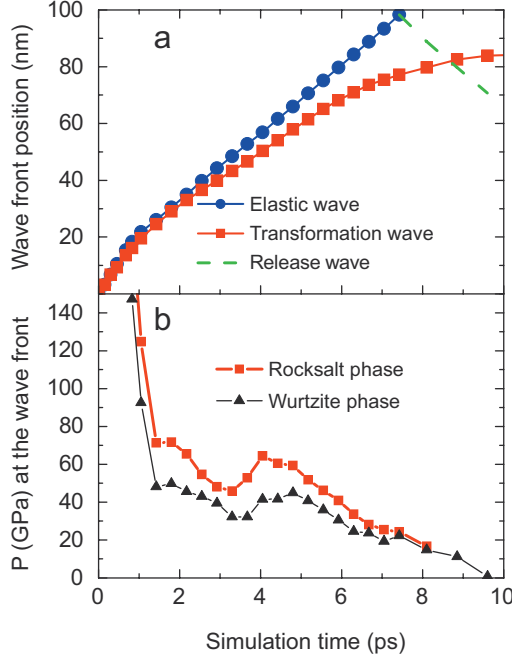
Fig. 9. (a) Shock wave front positions, along the *z*-direction in the mid of the *xy* plane, as a function of time, showing the increasing splitting of the initial overdriven wave into elastic (blue) and transformation (red) waves. The dashed green line shows the position of the release wave front, reflected from the back surface of the target. (b) Hydrostatic pressure calculated for the transformed (rocksalt phase) and untransformed atoms (wurtzite phase) in a 15 Å sphere at the transformation wave front position shown in (a).

of energy. From the initial hexagonal shape of the projectile front face and the measured energy transferred to the target the initial energy release is estimated to be $\sim 7.8 \times 10^5 \, \text{eV} \, \text{Å}^{-2} \, \text{ps}^{-1}$. The resulting high local energy density causes localized melting and vaporization (Belonoshko, 1997; Brannon and Chhabildas, 1995; Chhabildas et al., 2006; Holian, 1988), as well as large gradients in density, pressure, and temperature. This creates a strong shock wave that propagates nearly isotropically into the rest of the target, as the longitudinal sound speed of AlN (see Table 2) varies little for different crystallographic directions (see Fig. 8(b) and (c)).

During the first picosecond after impact, the average speed of the wave front is $\sim 19 \, \text{km/s}$. As the projectile deforms (Fig. 8(a) and (b)) and transfers its kinetic energy to the target, the shock wave loses its peak pressure (Fig. 8(b)), and accordingly the wave front speed decreases (Fig. 9(a)). The decrease in the wave front pressure transforms the initially overdriven wave profile (Kadau et al., 2002) into a split shock wave profile with an elastic wave traveling ahead of a SPT wave (Figs. 8(b), (c) and 9(a)). The elastic wave travels at $\sim 12 \, \text{km/s}$ and compresses the wurtzite crystal. Subsequently, the SPT wave drives the AlN crystal from the four-coordinated wurtzite structure to the more compact six-coordinated rocksalt structure. After the splitting, the SPT wave speed drops continuously until it halts at $\sim 8 \, \text{ps}$, resulting from the decreasing wave front pressure (Fig. 9(b)).

When the elastic compressive wave reaches the back free surface of the target, shown in Fig. 8(c), a release tensile wave is propagated back and when it reaches the SPT wave, at $\sim 8.5 \, \text{ps}$, it completely halts the vanishing structural transformation by fully releasing the compressive stress (Figs. 8(d), 9(a) and (b)). The advance of the interface between wurtzite and rocksalt phases in the *z*-direction after 8.5 ps shown in Fig. 9(a) is caused only by the displacement of the atoms due the residual linear momentum transferred from the projectile during the impact.

Fig. 8. Shock wave evolution during the simulation. Projectile atoms are shown in gray and the AlN target atoms are color-coded according to their pressures. Only a three-quarter cut of the target is shown to visualize the internal pressure distribution. The projectile is impacting the target from the right side. (a) Generation of the shock wave at 0.675 ps; (b) splitting of the initially overdriven shock wave into an elastic precursor (in light green) and a structural transformation wave (in dark green/yellow) at 5.325 ps; (c) elastic wave reaches the back free surface and transformation wave phases out at 7.650 ps; (d) the tensile wave propagates back and reach the transformation wave releasing the compression and halting the structural transformation at 9.150 ps.

### 4.2. Shock-induced structural phase transition

The theoretical transformation pressure of 25 GPa shown in Fig. 1(a) can be taken as the lower-bound pressure value for the transformation due to hysteresis. Usually in MD simulation, the pressure level for the transformation by homogeneous nucleation under static compression is higher than the lower-bound (Shimojo et al., 2000). However, the transformation in our case takes place by highly dynamic and heterogeneous mechanisms, and the pressure level to trigger and continue to transform the initial wurtzite crystal is expected to be close to the theoretical value. In fact, Fig. 9(b) shows that this is the case.

For planar and steady shock waves, the Hugoniot equations (Kadau et al., 2002) predict a jump in the pressure at the shock wave front. Although the shock wave is neither planar nor steady in our case we still observe a jump in the pressure at the transformation shock front in Fig. 9(b). This pressure jump is considerable until 7.5–8 ps, when the pressure level drops to a level below the theoretical value for the transformation and the transformation wave ceases to advance. Fig. 9(a) still shows the advance of the shock front until ∼10 ps. But this is a result of the residual flow of atoms, and no more atoms are being transformed.

The structure of the rocksalt volume left behind the SPT wave is heterogeneous and complex because of the strong gradients and rapidly changing stress conditions of the shock wave. However, radial distribution function (Fig. 10(a)) and bond–angle distributions (Fig. 10(b)) calculated for the six-coordinated atoms show that the material behind the transformation wave has a nearly perfect rocksalt structure, with a volume reduction of 19% from the original wurtzite lattice. This large reduction in volume causes increasing tension in the interface of the two structures, because of the lattice mismatch, and eventually breaks the interface of a growing rocksalt grain during the transformation from the wurtzite. However, in the central region where the shock wave is nearly planar it is possible to identify three alignments of the rocksalt grains, corresponding to three equivalent atomic displacement paths in the {0 0 0 1} plane. The cross section of the rocksalt phase along the projectile penetration path in Fig. 11 shows clearly the presence of rocksalt grains with its [1 0 0] crystal direction aligned with the original [1 $\bar{1}$ 0 0], [1 0 $\bar{1}$ 0], and [0 1 $\bar{1}$ 0] wurtzite directions. On the other hand, elsewhere in the transformed volume, the nearly spherical SPT wave gives rise to a heterogeneous structure of grains of different sizes and random orientations. This is shown in Fig. 12 in which only atoms in the rocksalt phase are visualized. Consequently, the SPT wave front (i.e. the wurtzite–rocksalt interface) has a very rough morphology and heterogeneous stress distribution (Fig. 12(a) and (c)). When the stress in the wave front starts to attenuate to a level not sufficient to drive the structural transition, the wurtzite–rocksalt interfacial region becomes a site for stress concentration and defect generation.

As the release of the compressive stress continues, the rocksalt phase becomes unstable and a reverse transformation to the four-coordinated phase starts to take place. Fig. 9(a) and (b) indicates in the central region, the transformation halts at ∼8.5 ps, but in the whole system, because of the spherical shape of the transformation wave, the number of six-coordinated atoms increase till 10.3 ps. We monitored the reverse transformation in the whole system calculating the number of six-coordinated atoms in the simulation. After the maximum number of atoms is reached at 10.3 ps, the reverse transformation take place quickly. At the end of the simulation, at 31.5 ps, only 21% of the transformed atoms are still in the rocksalt structure.

### 4.3. Shock-induced plasticity

The initial linear momentum of the projectile is mostly dissipated in the shock wave creation during its disintegration, and it is transmitted to the target as a nearly spherical wave, despite that a residual flow in the impact direction generates a localized shear stress between the regions surrounding the penetration path. When the release waves from the free surface maximize this shear stress, plastic deformation is generated at the wurtzite–rocksalt interface. The impact direction is aligned with the [0 0 0 1] direction of the wurtzite crystal, which is perpendicular to the basal plane, i.e. one of the slip planes for dislocations (Audurier et al., 1998a). Since the planes of the highest shear stress do not coincide with this basal plane, the shear stress cannot be released by nucleation and propagation of dislocations. Instead, it is released through rotational plasticity, i.e. generation of a series of dislocation dipoles with opposite Burgers vectors in the basal plane, creating a kink band (crystalline region with a different crystallographic orientation from the surrounding, see Fig. 13(a)) (Romanov and Vladimirov, 1992). The kink band nucleates at the SPT wave front and develops into a defect-
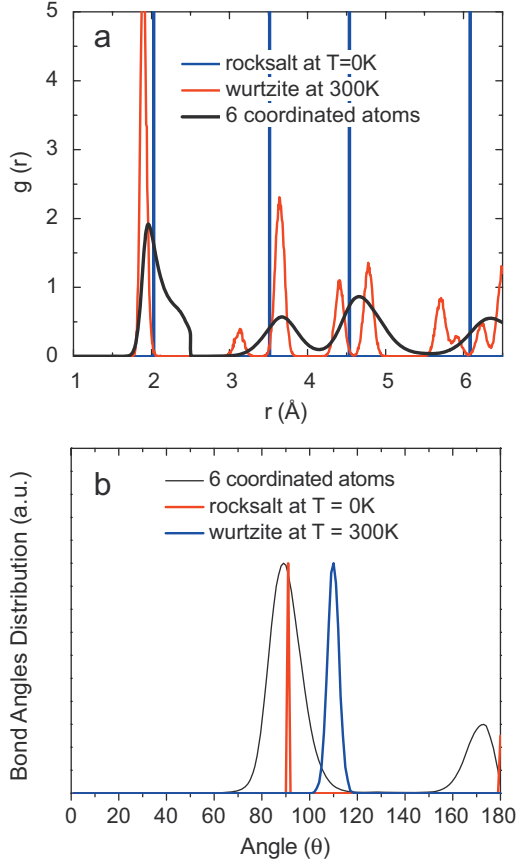
Fig. 10. (a) Radial distribution function and (b) bond angle distribution of six-coordinated atoms calculated during the simulation, showing the typical rocksalt structure. (a) and (b) also include reference data for a wurtzite crystal structure at $T = 300$ K and for a rocksalt crystal at $T = 0$ K with a 20% reduced volume. The first peak of the radial distribution function indicates a volume reduction of $\sim$19% from the initial wurtzite crystal. The bond angle distribution shows a peak around $88°$ close to the $90°$ of the perfect rocksalt and far from the $109.4°$ of the wurtzite tetrahedra. This agreement is excellent considering that the rocksalt phase was not considered in the fitting of the potential parameters. First peak of $g(r)$ for six-coordinated atoms in (a) presents a sharp drop because of the temperature broadening of the peaks and because six-coordinated atoms are defined as the atoms having six nearest-neighbors till 2.5 Å.

free wurtzite crystal (Fig. 13(a) and (b)). The dislocation dipoles in the basal planes forming the kink band are in fact closed dislocation loops (Fig. 13(a) and (b)). The dislocations lines, which form the boundary of the kink band, can move easily in the basal plane. To maximize the rotation and stress release, the dislocations on one side of the kink band align to form a superdislocation (Romanov and Vladimirov, 1992) (Fig. 13(b)) and a high-angle tilt boundary that glides to the edge of the system (Fig. 13(b)–(d)).

Fig. 14(a) and (b) shows a 3D view of the dislocations forming the kink band. The dislocations dipoles in the basal plane are in fact close dislocation loops with an edge dislocation component in the basal plane and a screw component perpendicular to it. Additionally, Fig. 14(b) shows that the dislocation loops are spread along the entire cross section of the target indicating that kink bands form a 3D structure surrounding the entire penetration path.

### 4.4. Microcrack nucleation and growth

The expansion of the target, along with the superposition of release waves, generates a growing tension in the target. This tension is concentrated at structural defects (Inglis, 1913) and eventually triggers the crack growth into the wurtzite crystal (Griffith, 1920). In our simulation, two independent mechanisms of crack nucleation and growth are identified, both rooted at the wurtzite–rocksalt interface. One mechanism is
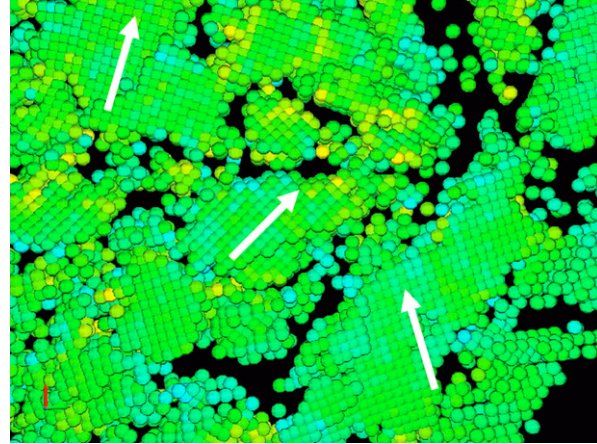
Fig. 11. Portion of the cross section of the system, at the central part of *xy* plane, inside the rocksalt-transformed volume. Arrows show the three different crystal orientation the rocksalt atoms assume after the transformation, indicating that the mechanism of transformation is based on atomic displacement on the $000\bar{1}$} plane in the three equivalent atomic displacement paths of the wurtzite crystal.

associated with the nanocavities nucleated in the wurtzite near the interface, and another associated with the high-angle tilt boundaries formed by superdislocations.

In the first mechanism, cracks nucleate at the nanocavities near the interface. These nanoscale voids are created in the overlap of the reflected tensile wave and the stress due to lattice mismatch and are formed by local detachment of Al–N bonds in $\{1\,\bar{1}\,0\,0\}$ planes, where the stress is maximum (see Fig. 15(a)). Fig. 16 shows the number of six member rings for the atoms on the nanovoids. The presence of atoms with six rings inside the nanocavities indicates their growth by a clean cleavage of the $\{1\,\bar{1}\,0\,0\}$ planes since atoms with six rings are characteristic on flat surfaces (see discussion in Section 3.3.3). These nanocavities further coalesce and form microcracks. To release the maximal tangential tension due to localized expansion, caused by the release wave, microcracks propagate along the $[0\,0\,0\,1]$ direction in mode I (opening mode) (see Fig. 15(b) and (c)), cleaving $\{1\,\bar{1}\,0\,0\}$ planes. Fig. 17(a) and (b) shows that all equivalent planes cleave following the spherical character of the shock wave and the stress profile.

In the second mechanism, the cracks are nucleated along the superdislocation boundary of the kink bands. After the superdislocation is optimally positioned in the basal plane to minimize, the shear stress of the target, it also becomes a spot for stress concentration. This concentration gives rise to nanovoids nucleation across the entire superdislocation line. When these nanovoids coalesce, the shear strength vanishes, allowing the target to relax the stress by crack propagation. This crack propagates mainly in mode II (shearing mode), releasing the shear stress, though a small mode I component is also present, as seen in Fig. 13(d). Fig. 17(c) shows the crack surface cleaved along the path defined by the superdislocation.

Fig. 18 shows cracks generated by both mechanisms in the end of the simulation at time 31.5 ps. Fragmentation of the target in the front surface is also seen in Fig. 18, following similar damage mechanisms discussed earlier.

## 5. Discussion

Experimentally, two major types of crack patterns are often associated with ceramic impacts: radial cracks and cone cracks (Chen et al., 2003; Sherman, 2000; Strassburger et al., 1994, 2000). The atomistic mechanism of damage initiation discussed earlier, along with the stress profile, can explain these two types of crack patterns. The radial cracks can be associated with the superposition of tangential stress from the spherical propagation of the compressive shock wave and release waves from the free surface. The cone cracks can be associated with the accumulation of shear stress during the particle flow, which in turn generates rotational plasticity preceding the crack development. Rotational plasticity (Romanov and Vladimirov, 1992) is commonly found in studies of damage in metals, where complex plastic deformation structures can be formed,
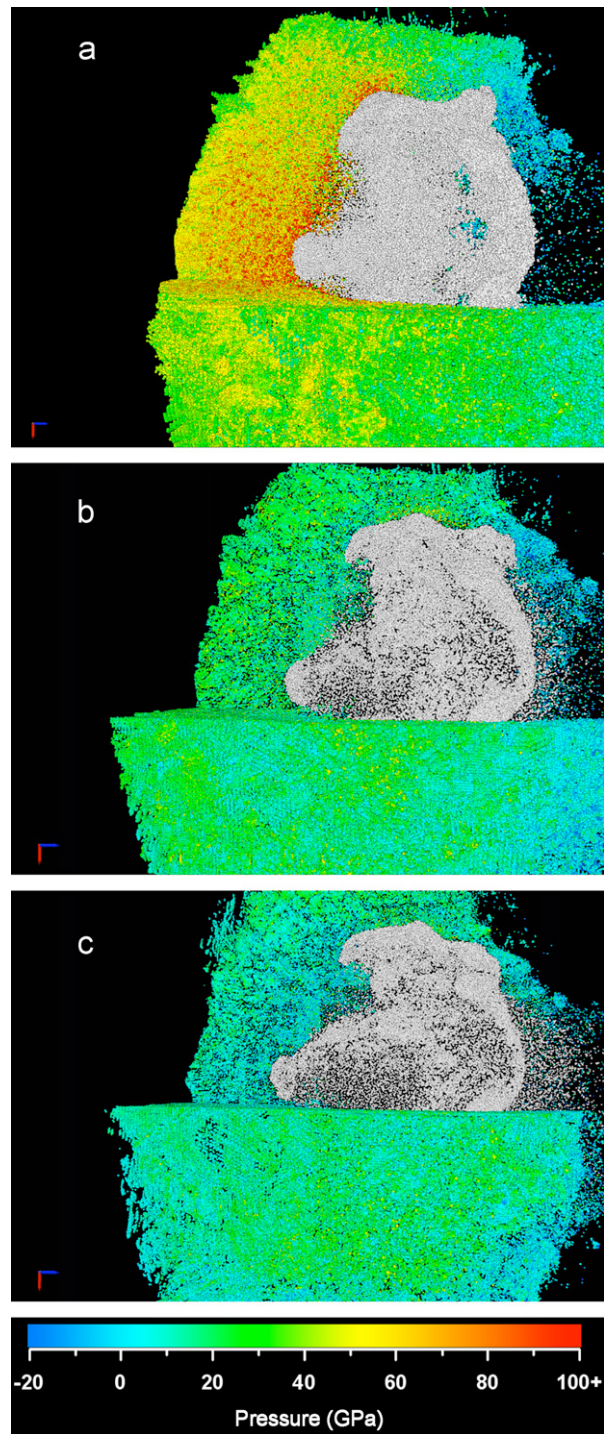
Fig. 12. Six-coordinated atoms transformed during the high pressure structural phase transition from wurtzite to rocksalt triggered by the shock wave. Only a three-quarter cut of the target is shown to visualize the internal structure. (a)–(c) show the evolution of the cluster of atoms transformed during the simulation run at (a) 5.325 ps, (b) 7.650 ps, and (c) 9.150 ps.

including dislocation loops, locks, twins, and kink bands. For brittle materials, plastic deformations are restricted, and failure generally occurs with no or little plastic deformation. However, plastic activity is enhanced at high temperatures or at high stress conditions (Audurier et al., 1998a, b; Azzaz et al., 2000; Seifert
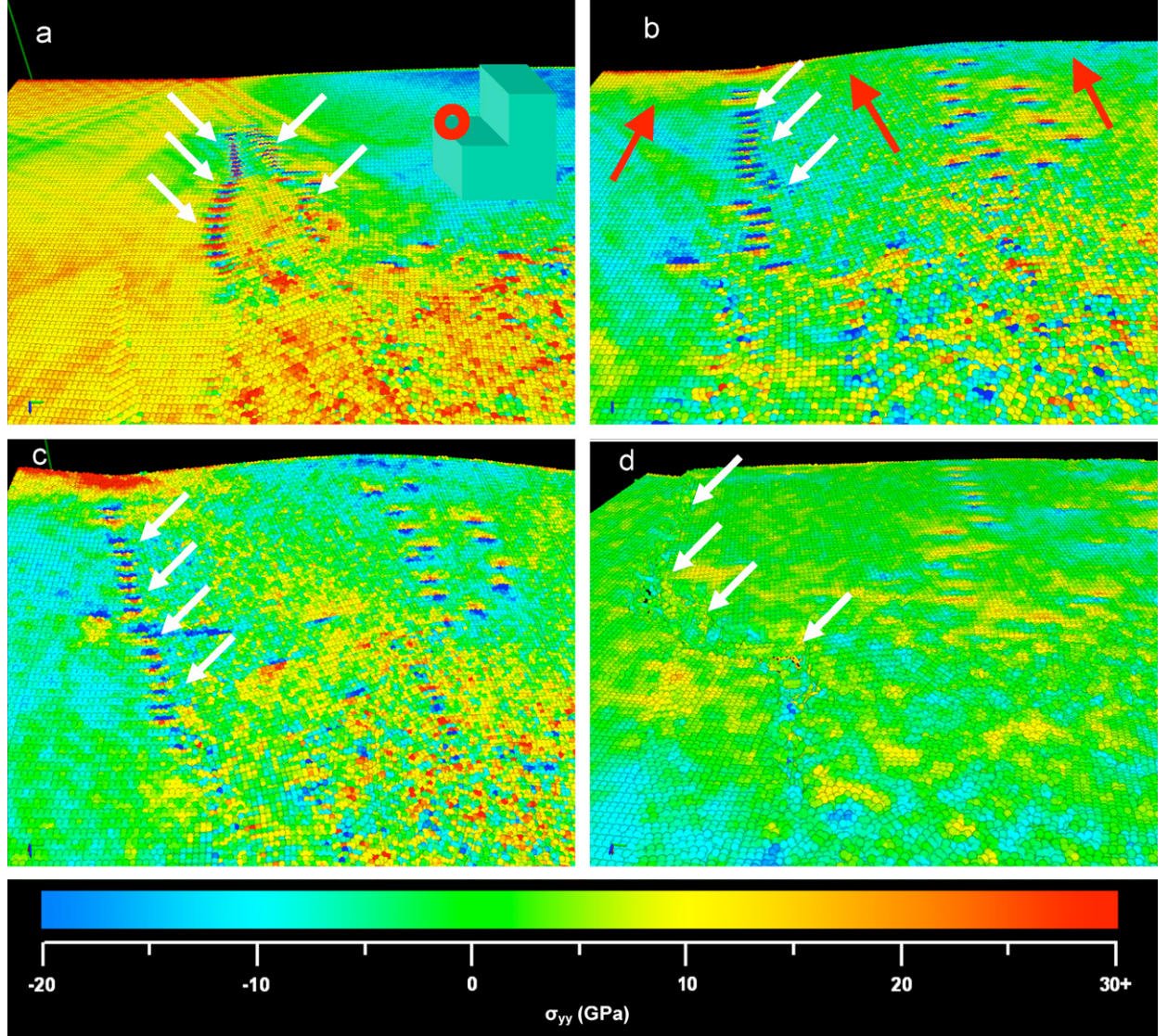
Fig. 13. Nucleation and development of a kink band from the wurtzite–rocksalt interface. Atoms are color-coded according to the $\sigma_{yy}$ component of stress with the color scale given in Fig. 4. Only the $(1\,\bar{1}\,0\,0)$ plane of the wurtzite crystal cut along the mid-part of the target is shown, as marked by the red circle in the inset. (a) The kink band nucleates at the interface and grows into the wurtzite crystal, generating dipoles of edge dislocations (shown by the arrows) with opposite Burgers vectors in the basal plane, and propagating in the $[1\,1\,\bar{2}\,0]$ direction at 11.10 ps. (b) The development of the kink band, with coordinated movement of dislocations (superdislocation) in the left side of the kink band at 15.30 ps. (c) Formation of a high angle tilt boundary from the superdislocation at 17.70 ps. (d) The tilt boundary formed is a stress concentrator and a favorable path for fracture, and it finally develops as a mode II shear fracture, with a small mode I component, displacing the grains and releasing the shear stress as shown at 31.50 ps.

et al., 1992; Yang et al., 2002), and rotational plasticity can be activated when the dislocations are not free to glide. Dislocation glides are limited either in the presence of barriers such as grain boundaries, impurities, or dislocation locks, or when the slip planes are not aligned with the high shear stress. In our case the later applies, as the high shear stress could be released activating dislocations in the $[0\,0\,0\,1]$ direction, which does not lay in any of the slip planes in the wurtzite (Audurier et al., 1998a, b). The kink bands define the future crack paths when the grain boundaries made of edge dislocations concentrate stress and create an energetically favorable path for cleavage. Our results show that plasticity plays an important role in the deformation, not only of metals and ductile compounds, but also of high-strength brittle ceramics, even at low temperature,
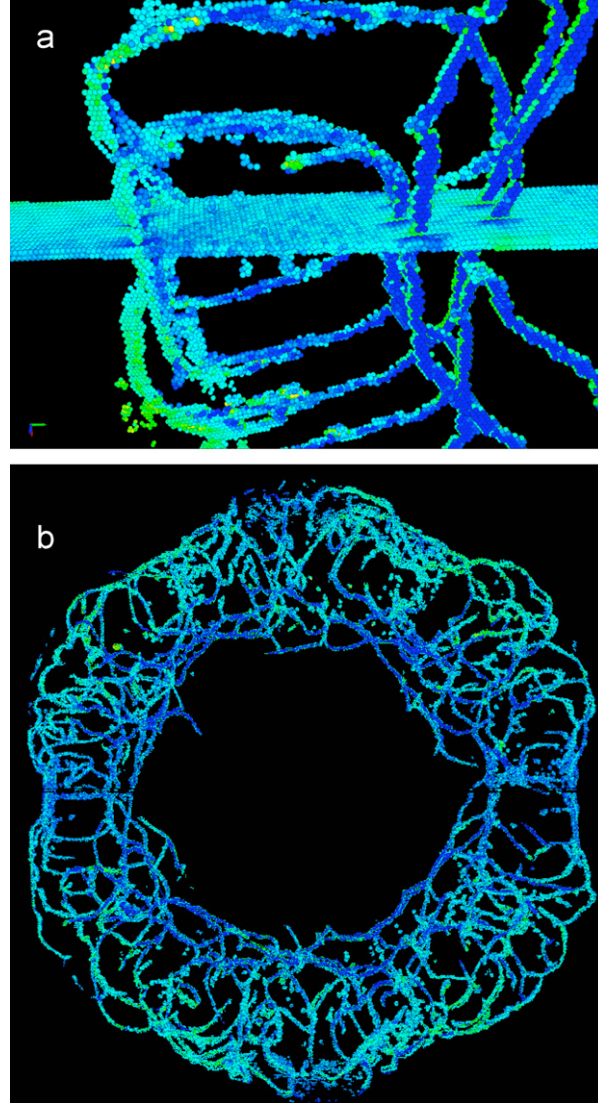
Fig. 14. A 3D representation of the kink band structure shown in Fig. 9(a)–(d). Only dislocations in a layer 100 Å thick from the back free surface is shown for clarity. (a) Shows the detailed 3D structure of dislocations showed in Fig. 9(b). The dislocation lines showed in Fig. 9(a)–(d) are in fact closed dislocation loops with and edge component in the [1 1 $\bar{2}$ 0] direction and a screw component along the [1 $\bar{1}$ 0 0] direction. (b) Shows the dislocation structures along the entire cross section of the target, showing that plastic deformations play an important role in the damage initiation and are spread around the entire penetration path.

when high stress gradients due to high-speed impacts are present. Under these conditions current experimental techniques cannot provide atomistic details of plastic activity preceding the development of cracks and the role of the SPT in the deformation process, although a few experiments already suggested this interplay (Lankford et al., 1998; Staehler et al., 2000). High performance launchers (Chhabildas et al., 1995; Thornhill et al., 2006) are under active development, but measurements of stress pulses and analysis of the deformation morphology remain a challenge. The stress pulse measurements are restricted by time and space resolution, though diagnostic techniques such as pulsed laser holography (Ang and Hansche, 1996) and ultra-fast flash-X-rays promise to be invaluable tools in the phenomenological description of the impact. Another phenomenon often observed in shock wave experiments is spallation (Ang and Hansche, 1996; Wagner et al., 1992), i.e. failure of material from the interaction with rarefaction waves, which is formed from the nucleation, growth and coalescence of nanocavities generating ductile fracture. This failure mechanism is not active in our simulation,
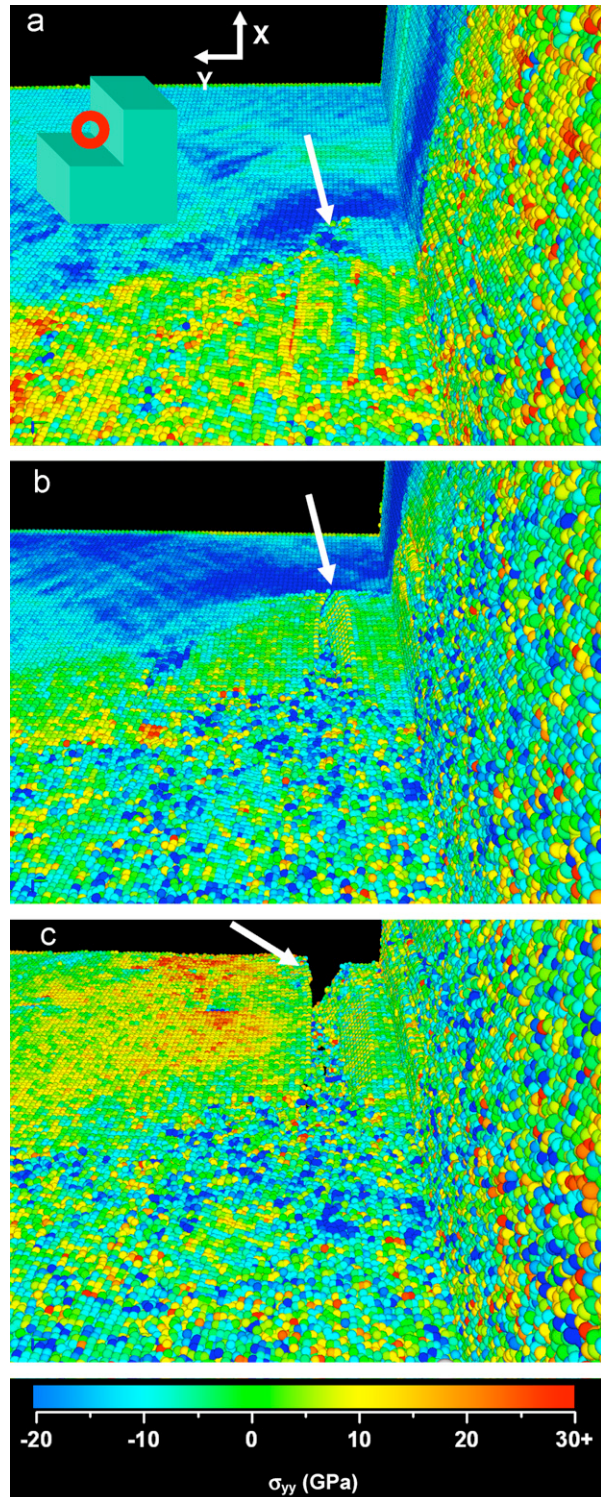
Fig. 15. Nucleation of a crack from a nanocavity near the wurtzite–rocksalt interface. Only part of the three-quarter target cut illustrated in Fig. 3 is shown here, at the location marked by the red circle in the inset. The atoms are color-coded according to the $\sigma_{yy}$ component of stress. (a) At 10.05 ps, the tensile release wave traveling in the wurtzite crystal reaches the rocksalt interface and starts to nucleate a nanocavity, shown by the white arrow. (b) At 12.0 ps, the wurtzite crystal is cleavage by the crack nucleated from the nanocavity, which propagates towards the back surface of the target. (c) At 16.95 ps, the crack reaches the back surface.
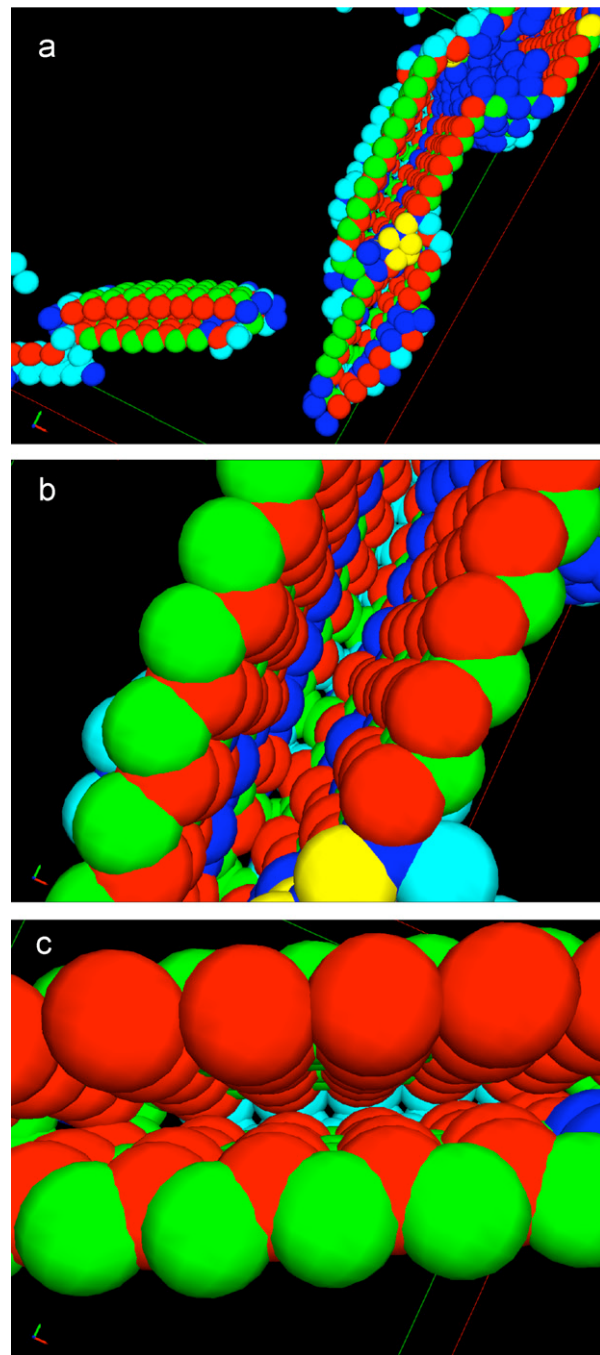
Fig. 16. Incipient nanovoids close to the interface of the wurtzite and rocksalt phases. Atoms were mined from the AlN wurtzite matrix based on the number of six member shortest-path rings. Color coding is the following. Atoms with 6 rings (red), 7–8 rings (blue), 9 rings (green), 10 rings (cyan). (b, c) Show the presence of atoms with six rings (red atoms) on the nanovoids internal surface indicating that growth is based on a clean cleavage of $\{1\bar{1}00\}$ planes inside the wurtzite crystal.

because the shock wave is rapidly attenuated during the spherical propagation, as opposed to the planar shock wave (Wagner et al., 1992), and the target is a very brittle ceramic.

Numerically, shock-impacted materials have been studied primarily by FEM (Bless and Rajendran, 1996; Holmquist et al., 2000a; Johnson et al., 1996), which use constitutive equations to describe the damage
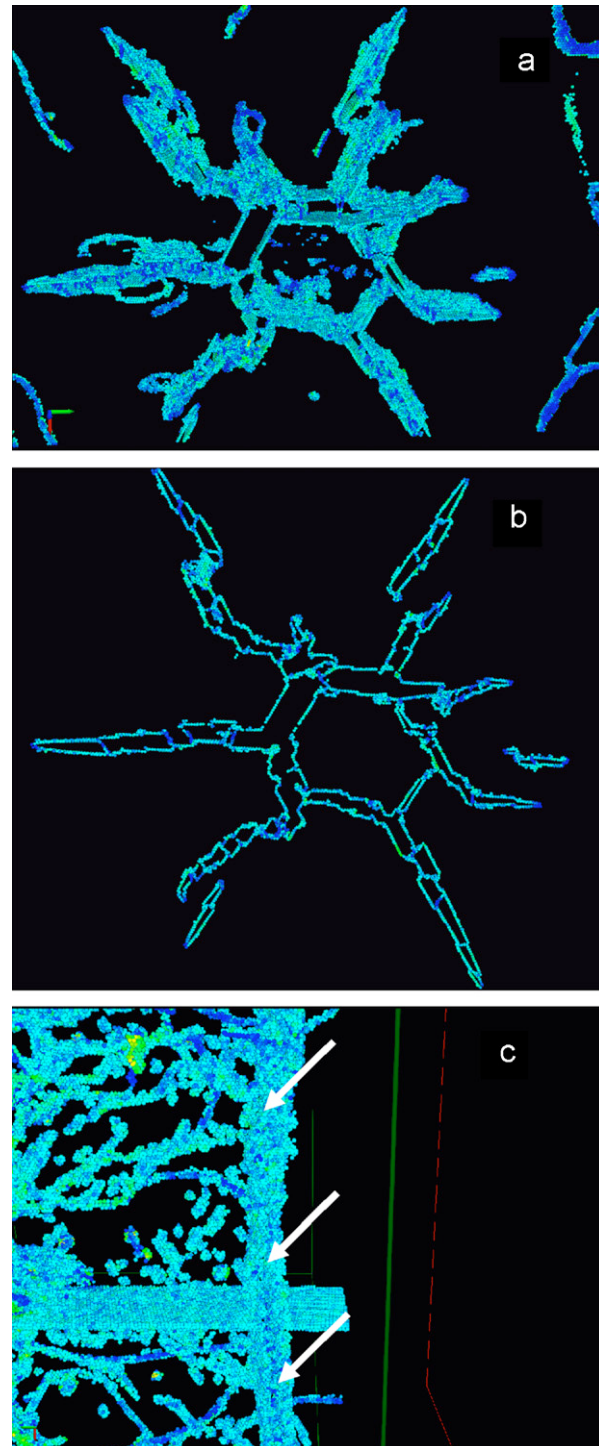
Fig. 17. (a, b) Show crack planes cleaved from nanocavities, as the one shown in Fig. 11(b) and (c). (a) Shows a 100 Å layer, while (b) shows a 10 Å layer to outline the cracks planes cleaved in the $[1\bar{1}00]$ direction of the wurtzite lattice. (c) 3D surfaces of the cracks nucleated from the kink band shown in Fig. 9(d), the white arrows indicate the cleaved plane.
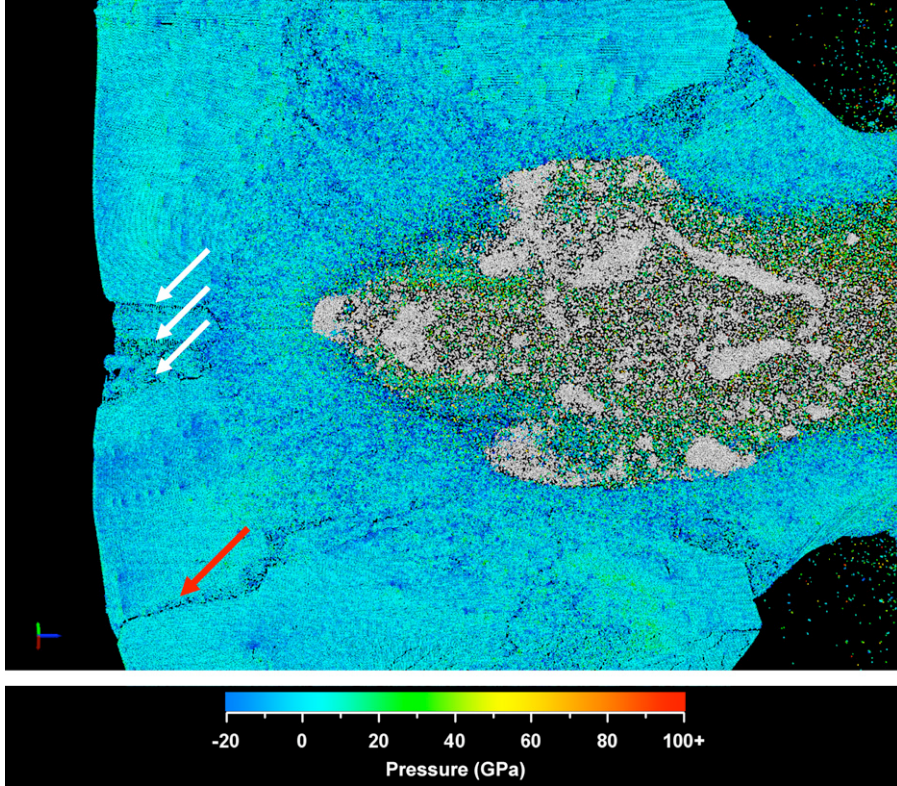
Fig. 18. AlN target after 31.5 ps from initial impact showing the multi-fractured configuration. White arrows indicate fractures cleaved from defects formed in the interface of the wurtzite and rocksalt structures. The red arrow indicates fracture in mode II, while the white arrows indicate fractures in mode I. Several other fractures, not discussed in the text, are also cleaved from similar mechanisms in the front surface of impact.

development based on the experimental material properties, configuration and stress conditions. FEM simulations can predict pressure, stresses, velocities, and the overall damage profile based on experimental inputs. Recent constitutive equations for AlN even account for the SPT during impact (Holmquist et al., 2000c). However, most of the constitutive models use static properties rather than the appropriate dynamic ones, obtained at the high strain rates of interest (Bless and Rajendran, 1996). Also they are not reliable in predicting crack nucleation, individual crack propagation, the dynamics of the structural transformation wave and its connection with crack nucleation, and the interface between the transformed and untransformed regions in AlN under impact. These atomistic mechanisms are naturally described by MD simulations. Constitutive equations could be extended to account for atomistic damage mechanisms provided from the MD simulations results, including the onset of rotational plasticity (Li et al., 2002), so that FEM simulations can provide the propagation of individual cracks and crack networks that may be initiated by impact.

MD simulations have provided the understanding of certain aspects of materials response to shock wave (Holian, 2002), but it is important to understand their limitations as well. In the case of hypervelocity impacts, for example, the region immediately adjacent to the impact contact reaches temperatures high enough to completely vaporize the atoms and create hot ionized plasma, which is not correctly modeled by empirical potentials. Fortunately, the hot plasma merely serves as a source of a shock pulse similar to laser-induced shock waves (Gilath, 1996), and the shock waves themselves are described accurately by interatomic potentials. The time and length scales that are accessible by MD simulations are also limited. Large-scale MD simulations, such as the present one, are restricted to the sub-nano-second time and sub-micron length scales. However, the study of shock wave damage initiation focused on the atomistic mechanisms at the nanoscale is accurately described by MD simulations as can be attested by the good agreement between the properties fitted by the interatomic potential function. Hybrid MD–FEM simulations (Abraham et al., 1998;

Lidorikis et al., 2001; Nakano et al., 2001; Ogata et al., 2001) could link the early stages of damage to the experimental profile of crack propagation.

## 6. Conclusions

The results presented highlight the vital role of large-scale MD simulations in elucidating the materials response to highly inhomogeneous and dynamic loading. With the interaction potential proposed the large-scale simulations are able to describe atomistic mechanisms of damage developed during a 15 km/s impact on AlN ceramics. It was observed that the impact induced strong shock wave splits into elastic and transformation wave components. This SPT wave drives a structural transformation from the wurtzite to the rocksalt phases of AlN. The SPT front wave induces plastic deformations, nanocavities, and kink bands that develop into modes I and II cracks, respectively. We have shown that different kinds of defects, such as, voids and dislocation structures, can be analyzed effectively through local average of virial stresses and shortest-path ring statistics.

With the availability of increasing computational power, larger MD simulations involving multi-billion atoms will be able to describe with complete atomistic details the dynamic response of polycrystalline compounds in any conceivable geometry of impact in the mesoscale length scales.

## References

Abraham, F.F., Broughton, J.Q., Bernstein, N., Kaxiras, E., 1998. Spanning the continuum to quantum length scales in a dynamic simulation of brittle fracture. Europhys. Lett. 44 (6), 783–787.

Allen, M.P., Tildesley, D.J., 1990. Computer Simulation of Liquids. Clarendon Press, Oxford.

Ang, J.A., Hansche, B.D., 1996. Pulsed holography diagnostics of impact fragmentation. In: Shahinpoor, M. (Ed.), High Pressure Shock Compression of Solids II: Dynamic Fracture and Fragmentation. Springer, New York, pp. 176–193.

Audurier, V., Demenet, J.L., Rabier, J., 1998a. ALN plastic deformation between room temperature and 800 degrees C-I. Dislocation substructure observations. Philos. Mag. A—Phys. Condens. Matter Struct. Defects Mech. Prop. 77 (4), 825–842.

Audurier, V., Demenet, J.L., Rabier, J., 1998b. AlN plastic deformation between room temperature and 800 degrees C-II. Dislocation core structures in basal and prismatic planes. Philos. Mag. A—Phys. Condens. Matter Struct. Defects Mech. Prop. 77 (4), 843–859.

Azzaz, M., Michel, J.P., Feregotto, V., George, A., 2000. TEM observations of dislocations in aluminium nitride after high temperature deformation. Mater. Sci. Eng. B—Solid State Mater. Adv. Tech. 71, 30–38.

Bachlechner, M.E., Omeltchenko, A., Nakano, A., Kalia, R.K., Vashishta, P., Ebbsjo, I., Madhukar, A., Messina, P., 1998. Multimillion-atom molecular dynamics simulation of atomic level stresses in Si(1 1 1)/Si3N4(0001) nanopixels. Appl. Phys. Lett. 72 (16), 1969–1971.

Beissel, S.R., Gerlach, C.A., Johnson, G.R., 2006. Hypervelocity impact computations with finite elements and meshfree particles. Int. J. Impact Eng. 33 (1–12), 80–90.

Belonoshko, A.B., 1997. Atomistic simulation of shock wave-induced melting in argon. Science 275 (5302), 955–957.

Bless, S.J., Rajendran, A.M., 1996. Initiation and propagation of damage caused by impact on brittle materials. In: Shahinpoor, M. (Ed.), High Pressure Shock Compression of Solids II: Dynamic Fracture and Fragmentation. Springer, New York, p. xvi, 483pp.

Bourne, N.K., 2006. Shock propagation through alumina observed at the mesoscale. J. Appl. Phys. 99 (2), 023502.

Branicio, P.S., Kalia, R.K., Nakano, A., Vashishta, P., 2006a. Shock-induced structural phase transition, plasticity, and brittle cracks in aluminum nitride ceramic. Phys. Rev. Lett. 96 (6), 065502.

Branicio, P.S., Rino, J.P., Shimojo, F., 2006b. High-pressure phases of InP: an ab initio and molecular-dynamics study. Appl. Phys. Lett. 88 (16), 161919.

Brannon, R.M., Chhabildas, L.C., 1995. Experimental and numerical investigation of shock-induced full vaporization of zinc. Int. J. Impact Eng. 17 (1–3), 109–120.

Brenner, D.W., Robertson, D.H., Elert, M.L., White, C.T., 1993. Detonations at nanometer resolution using molecular-dynamics. Phys. Rev. Lett. 70 (14), 2174–2177.

Campbell, T., Kalia, R.K., Nakano, A., Shimojo, F., Tsuruta, K., Vashishta, P., Ogata, S., 1999. Structural correlations and mechanical behavior in nanophase silica glasses. Phys. Rev. Lett. 82 (20), 4018–4021.

Chatterjee, A., Kalia, R.K., Nakano, A., Omeltchenko, A., Tsuruta, K., Vashishta, P., Loong, C.K., Winterer, M., Klein, S., 2000. Sintering, structure, and mechanical properties of nanophase SiC: a molecular-dynamics and neutron scattering study. Appl. Phys. Lett. 77 (8), 1132–1134.

Chen, M.W., McCauley, J.W., Hemker, K.J., 2003. Shock-induced localized amorphization in boron carbide. Science 299 (5612), 1563–1566.

Chen, M.W., McCauley, J.W., Dandekar, D.P., Bourne, N.K., 2006. Dynamic plasticity and failure of high-purity alumina under shock loading. Nat. Mater. 5 (8), 614–618.

Cheung, K.S., Yip, S., 1991. Atomic-level stress in an inhomogeneous system. J. Appl. Phys. 70 (10), 5688–5690.

Chhabildas, L.C., Kmetyk, L.N., Reinhart, W.D., Hall, C.A., 1995. Enhanced hypervelocity launcher—capabilities to 16 km/s. Int. J. Impact Eng. 17 (1–3), 183–194.

Chhabildas, L.C., Reinhart, W.D., Thornhill, T.F., Brown, J.L., 2006. Shock-induced vaporization in metals. Int. J. Impact Eng. 33 (1–12), 158–168.

Christensen, N.E., Gorczyca, I., 1993. Calculated structural phase-transitions of aluminum nitride under pressure. Phys. Rev. B 47 (8), 4307–4314.

Cohen, M.L., 1993. Predicting useful materials. Science 261 (5119), 307–308.

Cormier, J., Rickman, J.M., Delph, T.J., 2001. Stress calculation in atomistic simulations of perfect and imperfect solids. J. Appl. Phys. 89 (1), 99–104.

Deleeuw, S.W., He, H., Thorpe, M.F., 1985. Vibrational-spectra of rings in vitreous silica. Solid State Commun. 56 (4), 343–346.

Dovidenko, K., Oktyabrsky, S., Narayan, J., 1997. Characteristics of stacking faults in AlN thin films. J. Appl. Phys. 82 (9), 4296–4299.

Ebbsjo, I., Kalia, R.K., Nakano, A., Rino, J.P., Vashishta, P., 2000. Topology of amorphous gallium arsenide on intermediate length scales: a molecular dynamics study. J. Appl. Phys. 87 (11), 7708–7711.

Franzblau, D.S., 1991. Computation of ring statistics for network models of solids. Phys. Rev. B 44 (10), 4925–4930.

Gilath, I., 1996. Laser-induced spallation and dynamic fracture at ultra high strain rate. In: Shahinpoor, M. (Ed.), High Pressure Shock Compression of Solids II: Dynamic Fracture and Fragmentation. Springer, New York, pp. 90–120.

Goldfarb, D., Hao, J.X., Kai, S.R., 1991. Shortest-path algorithms using dynamic breadth-1st search. Networks 21 (1), 29–50.

Gorczyca, I., Christensen, N.E., Perlin, P., Grzegory, I., Jun, J., Bockowski, M., 1991. High-pressure phase-transition in aluminum nitride. Solid State Commun. 79 (12), 1033–1034.

Gorelskii, V.A., Zelepugin, S.A., Tolkachev, V.F., 2000. Experimental and numerical study of ceramics destruction by high-velocity impact. Chem. Phys. Rep. 18 (10–11), 2211–2217.

Griffith, A.A., 1920. The phenomena of rupture and flow in solids. Philos. Trans. R. Soc. Lond. A 221, 163.

Guttman, L., 1990. Ring structure of the crystalline and amorphous forms of silicon dioxide. J. Non-Crystal. Solids 116 (2–3), 145–147.

Herbert, M.K., Mandeville, J.C., Taylor, E.A., McDonnell, J.A.M., 2001. Analogies and differences between quasi-static indentation and hypervelocity impact morphologies on thin solar cells. Int. J. Impact Eng. 26 (1–10), 321–331.

Hohenberg, P., Kohn, W., 1964. Phys. Rev. 136, B864.

Hohler, V., Stilp, A.J., 1987. Hypervolocity impact of rod projectiles with L/D from 1 to 32. Int. J. Impact Eng. 5, 323–331.

Holian, B.L., 1987. Hypervelocity-impact phenomena via molecular-dynamics. Phys. Rev. A 36 (8), 3943–3946.

Holian, B.L., 1988. Modeling shock-wave deformation via molecular-dynamics. Phys. Rev. A 37 (7), 2562–2568.

Holian, B.L., 2002. What is a shock wave? The view from the atomic scale. In: Thadani, N.N. (Ed.), High-Pressure Shock Compression of Solids VI: Old Paradigms and New Challenges. Springer, New York, pp. 149–168.

Holian, B.L., Lomdahl, P.S., 1998. Plasticity induced by shock waves in nonequilibrium molecular-dynamics simulations. Science 280 (5372), 2085–2088.

Holian, B.L., Straub, G.K., 1979. Molecular-dynamics of shock-waves in 3-dimensional solids-transition from nonsteady to steady waves in perfect crystals and implications for the Rankine-Hugoniot conditions. Phys. Rev. Lett. 43 (21), 1598–1600.

Holian, B.L., Hoover, W.G., Moran, B., Straub, G.K., 1980. Shock-wave structure via non-equilibrium molecular-dynamics and Navier-Stokes continuum mechanics. Phys. Rev. A 22 (6), 2798–2808.

Holmquist, T.J., Johnson, G.R., 2006. Characterization and evaluation of boron carbide for plate-impact conditions. J. Appl. Phys. 100 (9), 093525.

Holmquist, T.J., Templeton, D.W., Bishnoi, K.D., 2000a. The ballistic behavior of layered ceramic: a computational study. In: ICES 2000, International Conference on Computational Engineering and Sciences. Los Angeles, CA.

Holmquist, T.J., Templeton, D.W., Bishnoi, K.D., 2000b. High strain constitutive modeling for the wurtzite phase of aluminum nitride. In: PLASTICITY 2000, 8th International Symposium on Plasticity and its Current Applications. Whistler, BC, Canada.

Holmquist, T.J., Templeton, D.W., Bishnoi, K.D., 2000c. High strain rate constitutive modeling of aluminum nitride including a first-order phase transformation. J. Phys. Iv 10 (P9), 21–26.

Holmquist, T.J., Templeton, D.W., Bishnoi, K.D., 2001. Constitutive modeling of aluminum nitride for large strain, high-strain rate, and high-pressure applications. Int. J. Impact Eng. 25 (3), 211–231.

Inglis, C.E., 1913. Stresses in a plate due to the presence of cracks and sharp corners. Trans. Inst. Naval Arch. 55, 219.

Iwanaga, H., Kunishige, A., Takeuchi, S., 2000. Anisotropic thermal expansion in wurtzite-type crystals. J. Mater. Sci. 35 (10), 2451–2454.

Johnson, G.R., Holmquist, T.J., 1999. Response of boron carbide subjected to large strains, high strain rates, and high pressures. J. Appl. Phys. 85 (12), 8060–8073.

Johnson, G.R., Stryk, R.A., Beissel, S.R., 1996. SPH for high velocity impact computations. Comput. Meth. Appl. Mech. Eng. 139 (1–4), 347–373.

Johnson, G.R., Beissel, S.R., Stryk, R.A., 2000. A generalized particle algorithm for high velocity impact computations. Comput. Mech. 25 (2–3), 245–256.

Kadau, K., Germann, T.C., Lomdahl, P.S., Holian, B.L., 2002. Microscopic view of structural phase transitions induced by shock waves. Science 296 (5573), 1681–1684.

Kalia, R.K., Nakano, A., Omeltchenko, A., Tsuruta, K., Vashishta, P., 1997a. Role of ultrafine microstructures in dynamic fracture in nanophase silicon nitride. Phys. Rev. Lett. 78 (11), 2144–2147.

Kalia, R.K., Nakano, A., Tsuruta, K., Vashishta, P., 1997b. Morphology of pores and interfaces and mechanical behavior of nanocluster-assembled silicon nitride ceramic. Phys. Rev. Lett. 78 (4), 689–692.

Karki, B.B., Stixrude, L., Wentzcovitch, R.M., 2001. High-pressure elastic properties of major materials of Earth's mantle from first principles. Rev. Geophys. 39 (4), 507–534.

Kipp, M.E., Grady, D.E., 1994. Shock phase-transformation and release properties of aluminum nitride. J. Phys. III 4 (C8), 249–256.

Kohn, W., Vashishta, P., 1983. In: March, S.L.a.N.H. (Ed.), Theory of Inhomogeneous Electron Gas. Plenum, New York, p. 79.

Kresse, G., Hafner, J., 1994. Ab-initio molecular-dynamics simulation of the liquid-metal amorphous-semiconductor transition in germanium. Phys. Rev. B 49 (20), 14251–14269.

Lankford, J., Predebon, W.W., Staehler, J.M., Subhash, G., Pletka, B.J., Anderson, C.E., 1998. The role of plasticity as a limiting factor in the compressive failure of high strength ceramics. Mech. Mater. 29 (3–4), 205–218.

Levinshteæin, M.E., Rumyantsev, S.L., Shur, M., 2001. Properties of Advanced Semiconductor Materials: GaN, AlN, InN, BN, SiC, SiGe. Wiley, New York.

Li, J., Van Vliet, K.J., Zhu, T., Yip, S., Suresh, S., 2002. Atomistic mechanisms governing elastic limit and incipient plasticity in crystals. Nature 418 (6895), 307–310.

Lidorikis, E., Bachlechner, M.E., Kalia, R.K., Nakano, A., Vashishta, P., Voyiadjis, G.Z., 2001. Coupling length scales for multiscale atomistics-continuum simulations: atomistically induced stress distributions in Si/Si3N4 nanopixels. Phys. Rev. Lett. 87, 8, article no. 086104.

Lutsko, J.F., 1988. Stress and elastic-constants in anisotropic solids-molecular-dynamics techniques. J. Appl. Phys. 64 (3), 1152–1154.

Maillet, J.B., Mareschal, M., Soulard, L., Ravelo, R., Lomdahl, P.S., Germann, T.C., Holian, B.L., 2001a. Uniaxial Hugoniostat: a method for atomistic simulations of shocked materials. Phys. Rev. E 6302 (2), 016121.

Maillet, J.B., Mareschal, M., Soulard, L., Ravelo, R., Lomdahl, P.S., Germann, T.C., Holian, B.L., 2001b. Uniaxial Hugoniostat: a method for atomistic simulations of shocked materials. Phys. Rev. E 6302, 2, article no. 016121.

Mashimo, T., Uchino, M., Nakamura, A., Kobayashi, T., Takasawa, E., Sekine, T., Noguchi, Y., Hikosaka, H., Fukuoka, K., Syono, Y., 1999. Yield properties, phase transition, and equation of state of aluminum nitride (AlN) under shock compression up to 150 GPa. J. Appl. Phys. 86 (12), 6710–6716.

Mcdonald, R.A., Tanner, W.G., Alexander, W.M., 1993. A comparison of hole size formation caused by a hypervelocity impact with a thin-film using molecular-dynamics and Cth. Int. J. Impact Eng. 14 (1–4), 509–518.

Millett, J.C.F., Bourne, N.K., Dandekar, D.P., 2005. Delayed failure in a shock-loaded silicon carbide. J. Appl. Phys. 97 (11), 113513.

Mota, R.C., Branicio, P.S., Rino, J.P., 2006. A dynamic pathway for the alkaline earth oxides B1 to B2 transformation. Europhys. Lett. 76 (5), 836–841.

Nakane, M., Shizawa, K., Takahashi, K., 2000. Microscopic discussions of macroscopic balance equations for solids based on atomic configurations. Arch. Appl. Mech. 70 (8–9), 533–549.

Nakano, A., Bachlechner, M.E., Kalia, R.K., Lidorikis, E., Vashishta, P., Voyiadjis, G.Z., Campbell, T.J., Ogata, S., Shimojo, F., 2001. Multiscale simulation of nanosystems. Comput. Sci. Eng. 3 (4), 56–66.

Ogata, S., Lidorikis, E., Shimojo, F., Nakano, A., Vashishta, P., Kalia, R.K., 2001. Hybrid finite-element/molecular-dynamics/electronic-density-functional approach to materials simulations on parallel computers. Comput. Phys. Commun. 138 (2), 143–154.

Omeltchenko, A., Bachlechner, M.E., Nakano, A., Kalia, R.K., Vashishta, P., Ebbsjo, I., Madhukar, A., Messina, P., 2000. Stress domains in Si(1 1 1)/a-Si3N4 nanopixel: ten-million-atom molecular dynamics simulations on parallel computers. Phys. Rev. Lett. 84 (2), 318–321.

Orphal, D.L., Franzen, R.R., Piekutowski, A.J., Forrestal, M.J., 1996. Penetration of confined aluminum nitride targets by tungsten long rods at 1.5–4.5 km/s. Int. J. Impact Eng. 18 (4), 355–368.

Orphal, D.L., Franzen, R.R., Charters, A.C., Menna, T.L., Piekutowski, A.J., 1997. Penetration of confined boron carbide targets by tungsten long rods at impact velocities from 1.5 to 5.0 km/s. Int. J. Impact Eng. 19 (1), 15–29.

Pandolfi, A., Conti, S., Ortiz, M., 2006. A recursive-faulting model of distributed damage in confined brittle materials. J. Mech. Phys. Solids 54 (9), 1972–2003.

Pechenik, A., Kalia, R.K., Vashishta, P., 1999. Computer-Aided Design of High-Temperature Materials. Oxford University Press, New York.

Perdew, J.P., Burke, K., Ernzerhof, M., 1996. Generalized gradient approximation made simple. Phys. Rev. Lett. 77 (18), 3865–3868.

Quan, X., Clegg, R.A., Cowler, M.S., Birnbaum, N.K., Hayhurst, C.J., 2006. Numerical simulation of long rods impacting silicon carbide targets using JH-1 model. Int. J. Impact Eng. 33 (1–12), 634–644.

Rapaport, D.C., 1991. Multimillion particle molecular-dynamics. 2. Design considerations for distributed-processing. Comput. Phys. Commun. 62 (2–3), 217–228.

Ravelo, R., Holian, B.L., Germann, T.C., Lomdahl, P.S., 2004. Constant-stress Hugoniostat method for following the dynamical evolution of shocked matter. Phys. Rev. B 70 (1), 014103.

Reaugh, J.E., Holt, A.C., Wilkins, M.L., Cunningham, B.J., Hord, B.L., Kusubov, A.S., 1999. Impact studies of five ceramic materials and Pyrex. Int. J. Impact Eng. 23 (1), 771–782.

Reed, E.J., Fried, L.E., Joannopoulos, J.D., 2003a. A method for tractable dynamical studies of single and double shock compression. Phys. Rev. Lett. 90 (23), 235503.

Reed, E.J., Fried, L.E., Joannopoulos, J.D., 2003b. A method for tractable dynamical studies of single and double shock compression. Phys. Rev. Lett. 90 (23).

Reed, E.J., Fried, L.E., Henshaw, W.D., Tarver, C.M., 2006. Analysis of simulation technique for steady shock waves in materials with analytical equations of state. Phys. Rev. E 74 (5), 056706.

Reinhart, W.D., Chhabildas, L.C., Vogler, T.J., 2006. Investigating phase transitions and strength in single-crystal sapphire using shock-reshock loading techniques. Int. J. Impact Eng. 33 (1–12), 655–669.

Rino, J.P., Ebbsjo, I., Kalia, R.K., Nakano, A., Vashishta, P., 1993. Structure of rings in vitreous $SiO_2$. Phys. Rev. B 47 (6), 3053–3062.

Rino, J.P., Ebbsjo, I., Branicio, P.S., Kalia, R.K., Nakano, A., Shimojo, F., Vashishta, P., 2004. Short- and intermediate-range structural correlations in amorphous silicon carbide: a molecular dynamics study. Phys. Rev. B 70 (4).

Riou, P., Denoual, C., Cottenot, C.E., 1998. Visualization of the damage evolution in impacted silicon carbide ceramics. Int. J. Impact Eng. 21 (4), 225–235.

Romanov, A.E., Vladimirov, V.I., 1992. Disclinations in crystalline solids. In: Nabarro, F.R.N. (Ed.), Dislocations and Disclinations. North-Holland Publ. Co., Amsterdam; NY, pp. 191–402.

Seifert, A., Berger, A., Muller, W.F., 1992. Tem of dislocations in AlN. J. Am. Ceram. Soc. 75 (4), 873–877.

Sharma, A., Kalia, R.K., Nakano, A., Vashishta, P., 2003a. Large multidimensional data visualization for materials science. Comput. Sci. Eng. 5 (2), 26–33.

Sharma, A., Nakano, A., Kalia, R.K., Vashishta, P., Kodiyalam, S., Miller, P., Zhao, W., Liu, X.L., Campbell, T.J., Haas, A., 2003b. Immersive and interactive exploration of billion-atom systems. Presence-Teleop. Virtual Environ. 12 (1), 85–95.

Sharma, A., Kalia, R.K., Nakano, A., Vashishta, P., 2004. Scalable and portable visualization of large atomistic datasets. Comput. Phys. Commun. 163 (1), 53–64.

Shen, L.H., Li, X.F., Ma, Y.M., Yang, K.F., Lei, W.W., Cui, Q.L., Zou, G.T., 2006. Pressure-induced structural transition in AlN nanowires. Appl. Phys. Lett. 89 (14), 141903.

Sheppard, L.M., 1990. Aluminum nitride—a versatile but challenging material. Am. Ceram. Soc. Bull. 69 (11), 1801–1812.

Sherman, D., 2000. Impact failure mechanisms in alumina tiles on finite thickness support and the effect of confinement. Int. J. Impact Eng. 24 (3), 313–328.

Shimojo, F., Ebbsjo, I., Kalia, R.K., Nakano, A., Rino, J.P., Vashishta, P., 2000. Molecular dynamics simulation of structural transformation in silicon carbide under pressure. Phys. Rev. Lett. 84 (15), 3338–3341.

Staehler, J.M., Predebon, W.W., Pletka, B.J., Subhash, G., 2000. Micromechanisms of deformation in high-purity hot-pressed alumina. Mater. Sci. Eng. A—Struct. Mater. Prop. Microstruct. Process. 291 (1–2), 37–45.

Stampfl, C., Van de Walle, C.G., 1998. Energetics and electronic structure of stacking faults in AlN, GaN, and InN. Phys. Rev. B 57 (24), R15052–R15055.

Strassburger, E., Senf, H., Rothenhausler, H., 1994. Fracture propagation during impact in 3 types of ceramics. J. Phys. Iv 4 (C8), 653–658.

Strassburger, E., Lexow, B., Beffort, O., Jeanquartier, R., 2000. Behaviour of Al2O3-Al ceramic metal composites under projectile impact. J. Phys. Iv 10 (P9), 605–610.

Szlufarska, I., Nakano, A., Vashishta, P., 2005. A crossover in the mechanical response of nanocrystalline ceramics. Science 309 (5736), 911–914.

Tadmor, E.B., Hai, S., 2003. A Peierls criterion for the onset of deformation twinning at a crack tip. J. Mech. Phys. Solids 51 (5), 765–793.

Tanguy, D., Mareschal, M., Lomdahl, P.S., Germann, T.C., Holian, B.L., Ravelo, R., 2003. Dislocation nucleation induced by a shock wave in a perfect crystal: molecular dynamics simulations and elastic calculations. Phys. Rev. B 68 (14).

Tasdemirci, A., Hall, I.W., 2007. Numerical and experimental studies of damage generation in multi-layer composite materials at high strain rates. Int. J. Impact Eng. 34 (2), 189–204.

Thornhill, T.F., Chhabildas, L.C., Reinhart, W.D., Davidson, D.L., 2006. Particle launch to 19 km/s for micro-meteoroid simulation using enhanced three-stage light gas gun hypervelocity launcher techniques. Int. J. Impact Eng. 33 (1–12), 799–811.

Todd, B.D., Evans, D.J., Daivis, P.J., 1995. Pressure tensor for inhomogeneous fluids. Phys. Rev. E 52 (2), 1627–1638.

Tsai, D.H., 1979. Virial theorem and stress calculation in molecular-dynamics. J. Chem. Phys. 70 (3), 1375–1382.

Tsuruta, K., Nakano, A., Kalia, R.K., Vashishta, P., 1998. Dynamics of consolidation and crack growth in nanocluster-assembled amorphous silicon nitride. J. Am. Ceram. Soc. 81 (2), 433–436.

Uehara, S., Masamoto, T., Onodera, A., Ueno, M., Shimomura, O., Takemura, K., 1997. Equation of state of the rocksalt phase of III-V nitrides to 72 GPa or higher. J. Phys. Chem. Solids 58 (12), 2093–2099.

Ueno, M., Onodera, A., Shimomura, O., Takemura, K., 1992. X-ray-observation of the structural phase-transition of aluminum nitride under high-pressure. Phys. Rev. B 45 (17), 10123–10126.

Vanderbilt, D., 1990. Soft self-consistent pseudopotentials in a generalized eigenvalue formalism. Phys. Rev. B 41 (11), 7892–7895.

Vashishta, P., Kalia, R.K., Rino, J.P., Ebbsjo, I., 1990. Interaction potential for $SiO_2$—a molecular-dynamics study of structural correlations. Phys. Rev. B 41 (17), 12197–12209.

Vashishta, P., Kalia, R.K., Ebbsjo, I., 1995. Low-energy floppy modes in high-temperature ceramics. Phys. Rev. Lett. 75 (5), 858–861.

Vogler, T.J., Chhabildas, L.C., 2006. Strength behavior of materials at high pressures. Int. J. Impact Eng. 33 (1–12), 812–825.

Wagner, N.J., Holian, B.L., Voter, A.F., 1992. Molecular-dynamics simulations of 2-dimensional materials at high-strain rates. Phys. Rev. A 45 (12), 8457–8470.

Walsh, P., Kalia, R.K., Nakano, A., Vashishta, P., Saini, S., 2000. Amorphization and anisotropic fracture dynamics during nanoindentation of silicon nitride: a multimillion atom molecular dynamics study. Appl. Phys. Lett. 77 (26), 4332–4334.

Wang, Z., Tait, K., Zhao, Y., Schiferl, D., Zha, C., Uchida, H., Downs, R.T., 2004. Size-induced reduction of transition pressure and enhancement of bulk modulus of AlN nanocrystals. J. Phys. Chem. B 108 (31), 11506–11508.

Wentzcovitch, R.M., da Silva, C., Chelikowsky, J.R., Binggeli, N., 1998. A new phase and pressure induced amorphization in silica. Phys. Rev. Lett. 80 (10), 2149–2152.

Wilkins, M.L., 1978. Mechanics of penetration and perforation. Int. J. Eng. Sci. 16 (11), 793–807.

Wright, A.F., 1997. Basal-plane stacking faults and polymorphism in AlN, GaN, and InN. J. Appl. Phys. 82 (10), 5259–5261.

Xia, Q., Xia, H., Ruoff, A.L., 1993. Pressure-induced rock-salt phase of aluminum nitride—a metastable structure at ambient condition. J. Appl. Phys. 73 (12), 8198–8200.

Yadav, S., Ravichandran, G., 2003. Penetration resistance of laminated ceramic/polymer structures. Int. J. Impact Eng. 28 (5), 557–574.

Yang, Z.Q., He, L.L., Ye, H.Q., 2002. The effect of ball milling on the microstructure of ceramic AlN. Mater. Sci. Eng. A—Structural Mater. Prop. Microstruct. Process. 323 (1–2), 354–357.

Yang, L., Ma, Y.M., Iitaka, T., Tse, J.S., Stahl, K., Ohishi, Y., Wang, Y., Zhang, R.W., Liu, J.F., Mao, H.K., Jiang, J.Z., 2006. Pressure-induced phase transformations in the Ba8Si46 clathrate. Phys. Rev. B 74 (24), 245209.

Zhakhovskii, V.V., Zybin, S.V., Nishihara, K., Anisimov, S.I., 1999. Shock wave structure in Lennard–Jones crystal via molecular dynamics. Phys. Rev. Lett. 83 (6), 1175–1178.

Zhang, C., Bansal, B., Branicio, P.S., Kalia, R.K., Nakano, A., Sharma, A., Vashishta, P., 2006. Collision-free spatial hash functions for structural analysis of billion-vertex chemical bond networks. Comput. Phys. Commun. 175, 339–347.